iScience

CellPress
OPEN ACCESS

Article

Loss of the polarity protein Par3 promotes dendritic spine neoteny and enhances learning and memory

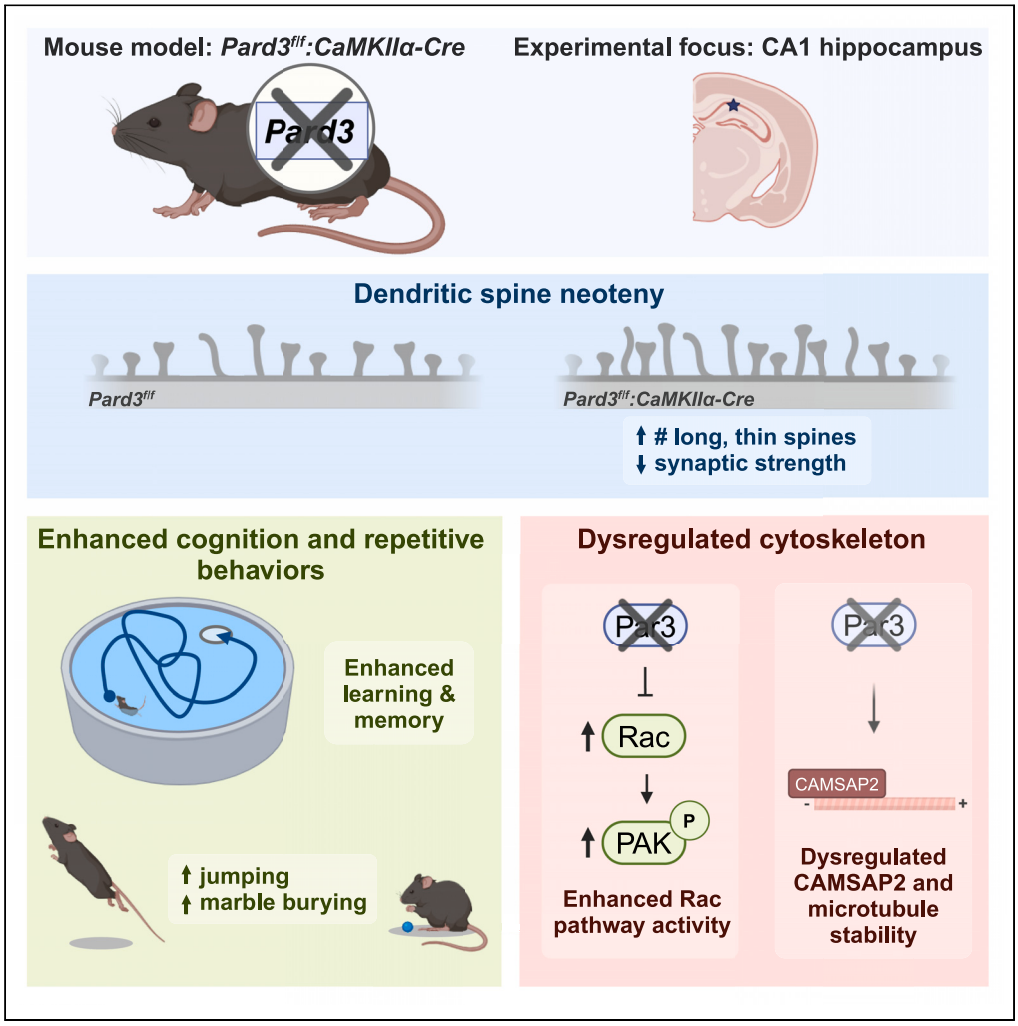

Mikayla M. Voglewede, Elif Naz Ozsen, Noah Ivak, ..., Miao Sun, Zhiping P. Pang, Huaye Zhang

huaye.zhang@rutgers.edu

Highlights

Par3 functions to limit the pool of immature spines

Loss of Par3 enhances spatial learning and memory and repetitive behavior

Loss of Par3 causes cytoskeletal dysregulation and enhances Rac activation

Par3 regulates CAMSAP2 phosphorylation and microtubule dynamics

Voglewede et al., iScience 27, 110308
July 19, 2024
https://doi.org/10.1016/j.isci.2024.110308

iScience

CellPress
OPEN ACCESS

Article

Loss of the polarity protein Par3 promotes dendritic spine neoteny and enhances learning and memory

Mikayla M. Voglewede,[1] Elif Naz Ozsen,[1] Noah Ivak,[2] Matteo Bernabucci,[1,3] Ruizhe Tang,[1] Miao Sun,[1] Zhiping P. Pang,[1,3] and Huaye Zhang[1,4,*]

SUMMARY

The Par3 polarity protein is critical for subcellular compartmentalization in different developmental processes. Variants of *PARD3*, encoding PAR3, are associated with intelligence and neurodevelopmental disorders. However, the role of Par3 in glutamatergic synapse formation and cognitive functions *in vivo* remains unknown. Here, we show that forebrain-specific Par3 conditional knockout leads to increased long, thin dendritic spines *in vivo*. In addition, we observed a decrease in the amplitude of miniature excitatory postsynaptic currents. Surprisingly, loss of Par3 enhances hippocampal-dependent spatial learning and memory and repetitive behavior. Phosphoproteomic analysis revealed proteins regulating cytoskeletal dynamics are significantly dysregulated downstream of Par3. Mechanistically, we found Par3 deletion causes increased Rac1 activation and dysregulated microtubule dynamics through CAMSAP2. Together, our data reveal an unexpected role for Par3 as a molecular gatekeeper in regulating the pool of immature dendritic spines, a rate-limiting step of learning and memory, through modulating Rac1 activation and microtubule dynamics *in vivo*.

INTRODUCTION

Dendritic spines are small, highly polarized protrusions on neurons serving as sites for most excitatory postsynaptic input. Plasticity of dendritic spines is necessary for learning,[1–7] while stable dendritic spines are thought to encode long-term memories.[8] In the dendritic spine head, the protein rich postsynaptic density (PSD) serves as the incoming signaling center opposing the presynaptic terminal. The PSD contains neurotransmitter receptors and signaling molecules crucial for synaptic transmission,[9] making it a distinct zone compared to the cytoskeleton-rich dendritic spine neck and dendritic shaft. Both actin and microtubules provide structure and contribute to the function of the compartmentalized domains within the dendritic spine.[10,11] However, the molecular mechanisms governing the cytoskeletal dynamics in the morphogenesis of these polarized spine structures remain incomplete.

The partitioning defective (Par) polarity complex, including Par3, a scaffolding molecule, Par6, an adaptor molecule, and atypical protein kinase C (aPKC), is responsible for establishing cell polarity in various cellular contexts, such as apical-basal compartmentalization and planar cell polarity.[12–14] In primary hippocampal neurons, knockdown of Par3 or Par6 causes a drastic shift to immature dendritic spines with a loss of presynaptic partners.[15,16] Par3 directly interacts with TIAM1, a guanine nucleotide exchange factor for Rac GTPases, to restrict Rac activity to the dendritic spines.[15] Together, Par3 and TIAM1 are recruited to the synapses by and directly interact with the adhesion GPCR, brain-specific angiogenesis inhibitor 1 (BAI1).[17] In addition, double conditional knockout of both aPKC isozymes, PKCι/λ and PKCζ, leads to impaired learning and memory.[18]

Interestingly, a copy number variant of *PARD3*, which encodes PAR3, is associated with autism spectrum disorder (ASD).[19] Various single nucleotide polymorphisms (SNPs) of *PARD3* are associated with schizophrenia,[20] intelligence,[21] education attainment,[22] and high math ability.[22] Similarly, *PARD3B*, a paralog of *PARD3*, is a strong candidate gene for ASD.[23–27] This suggests that PAR3 may play a key role in higher cognition and behavior. However, the *in vivo* role for Par3 in synaptic function and cognition remains completely unknown. Thus, we created a conditional knockout mouse model to postnatally knockout *Pard3* in forebrain excitatory neurons to investigate the role of Par3 in dendritic spine morphogenesis and learning and memory *in vivo*. Here, we show the loss of Par3 *in vivo* creates excess immature dendritic spines in the CA1 of the hippocampus and leads to a significant decrease in the amplitude of miniature excitatory postsynaptic currents (mEPSCs). Interestingly, the loss of Par3 enhances spatial learning and memory and repetitive behavior. Furthermore, we found the loss of Par3 dysregulates

[1]Department of Neuroscience and Cell Biology, Robert Wood Johnson Medical School, Rutgers, The State University of New Jersey, Piscataway, NJ 08854, USA
[2]Department of Cell Biology and Neuroscience, Rutgers, The State University of New Jersey, Piscataway, NJ 08854, USA
[3]The Child Health Institute of New Jersey, Robert Wood Johnson Medical School, Rutgers, The State University of New Jersey, New Brunswick, NJ 08901, USA
[4]Lead contact
*Correspondence: huaye.zhang@rutgers.edu
https://doi.org/10.1016/j.isci.2024.110308

the Rac1 pathway and CAMSAP2-mediated microtubule dynamics. These data reveal a surprising role for Par3 in regulating a rate-limiting step of learning and memory through limiting the pool of immature dendritic spines.

RESULTS

Generating the *Pard3* conditional knockout model

To examine the effects of Par3 on dendritic spine morphogenesis and learning and memory *in vivo*, we established a *Pard3* conditional knockout mouse model by crossing *Pard3*$^{<tm1a(KOMP)Wtsi>}$/H mice with *CAG-Flpo* mice. The resulting *Pard3*$^{f/f}$ line (Tm1c) was crossed with *CaMKIIα-Cre* line through which Cre excises exons 8 and 9 of *Pard3* (Figure S1A). Since Par3 plays a role in establishing neuronal polarity[28] and to avoid early developmental defects, *CaMKIIα-Cre* was chosen to knockout *Pard3* two to three weeks postnatally. Experiments were carried out in 5- to 7-week-old mice. The presence of floxed *Pard3* gene was validated via PCR (Figure S1B). Cre expression was confirmed by crossing the *Pard3*$^{f/f}$ and *Pard3*$^{f/f}$*:CaMKIIα-Cre* mice with B6.129X1-*Gt(ROSA)26Sor*$^{tm1(EYFP)Cos}$/J, in which enhanced yellow fluorescent protein (EYFP) is expressed in *Cre*-expressing tissue. CaMKIIα-Cre is highly expressed in the hippocampus, specifically the CA1, with sparse cortical expression (Figure S1C), supporting previous publications using *CaMKIIα-Cre*.[29,30] Ablation of the Par3 protein was confirmed both *in vitro* and *in vivo* (Figures S1D–S1G). Additionally, conditional knockout of Par3 did not alter body weight (Figure S1H). This novel mouse model provides a unique opportunity to investigate the role of Par3 in dendritic spines and cognition *in vivo*.

Loss of Par3 promotes neoteny of dendritic spines

In vitro shRNA-mediated knockdown of Par3 in primary hippocampal neurons results in an increase in immature, filopodia-like spines and a decrease in mature dendritic spines.[15] By contrast, the loss of Par3 *in vivo* increases the density of dendritic spines in the stratum radiatum layer of hippocampal CA1 pyramidal neurons in both male and female mice at 5 weeks old (Figures 1A, 1B, S2A, and S2B, males: $p = 0.0226$; females: $p = 0.0246$). Interestingly, WT female mice exhibit higher density of dendritic spines compared to age-matched males, which is consistent with previous reports showing higher dendritic spine density in proestrus females compared to males,[31] even though estrous cycle was not determined in our experiments. Overall, our results demonstrate that loss of Par3 increases dendritic spine density regardless of sex.

We then analyzed dendritic spine morphology in *Pard3*$^{f/f}$ and *Pard3*$^{f/f}$*:CaMKIIα-Cre* hippocampi. Dendritic spine length (Figure 1C) and spine head width (Figure 1D) were used to calculate length to width ratio (LWR, Figure 1E) in *Pard3*$^{f/f}$ and *Pard3*$^{f/f}$*:CaMKIIα-Cre* males. The length, width, and LWR were used to classify spines into morphological categories. The loss of Par3 results in longer spines (Figure 1C, $p = 0.0149$) with an increased LWR (Figure 1E, $p = 0.0033$) but no significant change in spine head width (Figure 1D). The increased LWR of *Pard3*$^{f/f}$*:CaMKIIα-Cre* dendritic spines is characteristic of a shift to long, thin spines more commonly found in early development. Surprisingly, the density of mushroom dendritic spines did not change. However, there was an increase in filopodia spines (Figure 1F, $p = 0.0027$) and a trend toward increased long thin dendritic spines (Figure 1F, $p = 0.1075$). Together, this indicates the loss of Par3 results in a shift toward longer, thinner dendritic spines and increased dendritic spine density commonly found in early development prior to synaptic refinement and maturation.

We next aimed to determine how the extra pool of long, thin dendritic spines alter synaptic protein expression and function. We isolated PSD-enriched fractions from hippocampal tissue using centrifugation (Figure S2C). Although the complete elimination of the presynaptic membrane does not occur, PSD-related proteins are enriched providing a cleaner investigation of postsynaptic changes (Figure S2D). In the PSD-enriched fraction, the loss of Par3 does not result in altered synaptic levels of proteins including SH3 and multiple ankyrin repeat domains 3 (Shank3), post synaptic density protein 95 (PSD-95), homer scaffold protein 1 (Homer1), N-methyl-D-aspartate receptor subunit 1 (NMDAR1), AMPA-type glutamate receptor subunit 1 (GluR1), or subunit 2 (GluR2) (Figures 1G and 1H). Drawing a definite conclusion is challenging because the PSD-enriched fraction may not encompass the surplus of filopodia and long thin dendritic spines, which normally have minimal or no PSDs. Thus, the similar synaptic protein expression could be due to similar density of mature dendritic spines (Figure 1F), or it could be due to similar amounts of synaptic proteins spread across the increased dendritic spine density. Finally, we observed no significant changes in the synaptic levels of total or active aPKC (Figures S2E and S2F).

Next, our objective was to investigate potential changes in synaptic transmission in the *Pard3*$^{f/f}$*:CaMKIIα-Cre* mice. Basal excitatory synaptic transmission was measured by recording mEPSCs in the CA1 of the hippocampus of 5- to 7-week-old mice. Interestingly, we found a significant decrease in the amplitude of mEPSCs with no significant changes in mEPSC frequency in the *Pard3*$^{f/f}$*:CaMKIIα-Cre* hippocampus (Figures 1I and 1J, amplitude: $p = 0.0271$), which suggests the loss of Par3 in the hippocampus decreases synaptic strength. This decrease in mEPSC amplitude is consistent with the observation that *Pard3*$^{f/f}$*:CaMKIIα-Cre* neurons have increased density of filopodia and long thin spines. Since these immature synaptic features are common in early postnatal development, our data suggest the loss of Par3 promotes dendritic spine neoteny, leading to the retention of immature synaptic features in early adulthood.

Loss of Par3 enhances learning and memory

We next investigated whether the increase in immature dendritic spines alters cognitive function, specifically hippocampal-dependent spatial learning via the Morris Water Maze (MWM). In the MWM mice underwent 5 trials per day on 4 consecutive training days to learn the location of a hidden platform in opaque water using spatial cues. 24 h after the last training day, memory was tested during the probe test. In the probe test the platform was removed and mice swam for 60 s. Surprisingly on training day 2 of the MWM, *Pard3*$^{f/f}$*:CaMKIIα-Cre* mice reached the

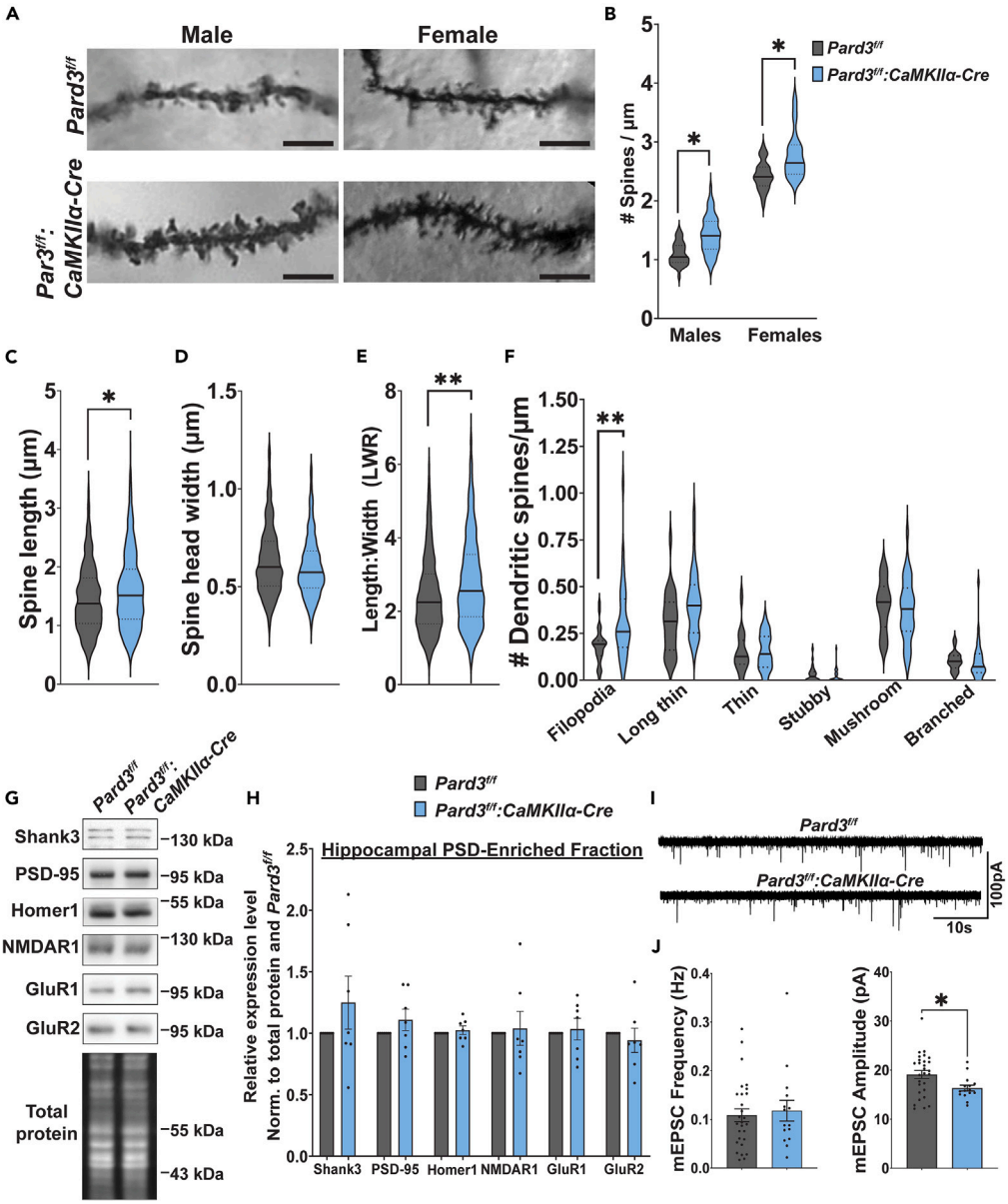

Figure 1. Loss of Par3 increases density of longer, thinner dendritic spines and alters synaptic function

(A) Representative images of *Pard3*$^{f/f}$ (top) and *Pard3*$^{f/f}$*:CaMKIIα-Cre* (bottom) dendritic spines. Scale bar = 5 µm.

(B) Quantification of dendritic spine density. *N* = 38 total dendrites from 3 *Pard3*$^{f/f}$ males, 58 total dendrites from 5 *Pard3*$^{f/f}$*:CaMKIIα-Cre*, males, 30 total dendrites from 3 *Pard3*$^{f/f}$ females, and 29 total dendrites from 3 *Pard3*$^{f/f}$*:CaMKIIα-Cre* females.

(C–E) Quantification of (C) spine length, (D) spine head width, (E) length to width ratio (LWR). *N* = 1164 total spines from 3 *Pard3*$^{f/f}$ mice and 1407 total spines from 5 *Pard3*$^{f/f}$*:CaMKIIα-Cre* mice.

(F) Quantification of morphology classification. *N* = 30 total dendrites from 3 *Pard3*$^{f/f}$ mice and 36 total dendrites from 5 *Pard3*$^{f/f}$*:CaMKIIα-Cre* mice. In B-F, data representation includes violin plots with thick lines as medians and dotted lines as quartiles. Data are analyzed via mixed model analysis. *$p \leq 0.05$, **$p \leq 0.01$.

(G) Representative images of Western blots of proteins detected from PSD-enriched fractions derived from *Pard3*$^{f/f}$ or *Pard3*$^{f/f}$*:CaMKIIα-Cre* hippocampal tissue.

(H) Quantification of relative levels of proteins in PSD-enriched fractions normalized to total protein and to *Pard3*$^{f/f}$ including SH3 and multiple ankyrin repeat domains 3 (Shank3), postsynaptic density protein 95 (PSD-95), homer scaffold protein 1 (Homer1), N-methyl-D-aspartate receptor subunit 1 (NMDAR1), glutamate ionotropic receptor AMPA type subunit 1 (GluR1) and 2 (GluR2). *N* = 7 *Pard3*$^{f/f}$ mice and 7 *Pard3*$^{f/f}$*:CaMKIIα-Cre* mice.

(I) mEPSC traces and (J) quantification of mEPSC frequency and amplitude. *N* = 28 *Pard3*$^{f/f}$ cells and 15 *Pard3*$^{f/f}$*:CaMKIIα-Cre* cells. In (H) and (J) all data are presented as individual mice or cells as points and bar graphs as mean ± SEM, analyzed with unpaired t-test. *$p \leq 0.05$.

See also Figure S2.

hidden platform ~39% more quickly than *Pard3*$^{f/f}$ mice (Figure 2A, day 2: $p = 0.0191$), suggesting either they retained a stronger memory of the platform location from training day 1 and/or their learning capacity was enhanced. This was not due to increased exposure leading to enhanced learning and memory, as *Pard3*$^{f/f}$ and *Pard3*$^{f/f}$*:CaMKIIα-Cre* exhibited similar swimming velocities during all training days (Figure S3C). Throughout the training period, there were no significant sex differences (Figures S3A and S3B). During the probe test, both *Pard3*$^{f/f}$ and *Pard3*$^{f/f}$*:CaMKIIα-Cre* learned the location of the platform as indicated by spending similar amounts of time in the target quadrant where the platform was previously located, as well as similar latency to platform location, similar levels of platform location crossings, and similar cumulative distances from the platform location (Figures 2B–2F).

Given that *Pard3*$^{f/f}$*:CaMKIIα-Cre* mice only showed significantly improved performance during one day of the MWM training, we wanted to increase the difficulties of the learning task to see whether *Pard3*$^{f/f}$*:CaMKIIα-Cre* mice show enhanced performance compared with controls. As such, we reduced the training trials from 5 trials per day to 3 trials per day. *Pard3*$^{f/f}$*:CaMKIIα-Cre* mice show a trend for reaching the platform more quickly than the *Pard3*$^{f/f}$ mice in days 3 and 4 during the hidden platform training (Figure 2G); however this did not reach statistical significance. Interestingly, during the probe test, although the overall time spent in the target quadrant was not significantly different between *Pard3*$^{f/f}$ and *Pard3*$^{f/f}$*:CaMKIIα-Cre* mice (Figures 2H, 2I, and S3E–S3H), *Pard3*$^{f/f}$*:CaMKIIα-Cre* mice show significantly reduced latency to the platform location (Figure 2J, $p = 0.0251$), increased number of the platform location crossings (Figure 2K, $p = 0.0003$), and reduced cumulative distance to platform location (Figure 2L, $p = 0.0275$). These data suggest that in this more difficult version of the MWM test, *Pard3*$^{f/f}$*:CaMKIIα-Cre* mice show significantly enhanced spatial learning and memory as compared with *Pard3*$^{f/f}$ mice.

Loss of Par3 increases repetitive behaviors without altering social or anxiety-like behaviors

Interestingly, we observed a significant behavioral difference during the MWM training sessions. After successfully reaching the platform, some mice attempted jumping from the platform toward the maze wall. Surprisingly, 54.5% of the *Pard3*$^{f/f}$*:CaMKIIα-Cre* mice jumped from the platform, nearly all of which jumped during 3 or more trials. Only 21% of *Pard3*$^{f/f}$ mice jumped from the platform, nearly all of which jumped at the end of only a single trial. Overall, *Pard3*$^{f/f}$*:CaMKIIα-Cre* mice attempted jumping at the end of more trials than *Pard3*$^{f/f}$ (Figure 3A, $p = 0.0446$). This is intriguing as repeated jumping behavior has been observed in ASD mouse models such as the Shank2 knockout mice.[32]

To further explore whether *Pard3*$^{f/f}$*:CaMKIIα-Cre* mice exhibit repetitive behaviors, we performed marble burying test, which reflects repetitive and perseverative behaviors.[33] Mice were individually placed in large cages with a 4x5 array of glass marbles laid on top of a layer of fresh, pelleted cellulose bedding. Mice were allowed to stay in the cage for 30 min and the number of marbles buried were scored (Figure 3B). We found that *Pard3*$^{f/f}$*:CaMKIIα-Cre* mice buried over twice as many marbles as compared with their littermate controls (Figure 3C, $p = 0.002$). This suggests the loss of Par3 in forebrain excitatory neurons leads to an increase in repetitive behaviors.

Repetitive behavior is a hallmark of ASD, and the Par3 family proteins are associated with ASD.[19,23–27] Thus, we decided to further explore the effects of forebrain Par3 ablation on ASD-related behaviors including anxiety-like behavior and social interactions. To examine anxiety-like behaviors, we performed the elevated plus maze (EPM) and open field test (OFT). Mice have an innate aversion to bright, open spaces. In the EPM test, a plus shaped maze consisting of two enclosed arms and two open arms was elevated above the ground (Figure 3D). Usually, mice spend less time in the open, exposed arms. Similarly, in the OFT, a square plexiglass chamber was placed under a bright light. Mice typically spend more time in the outer edge of the chamber as opposed to the open, exposed center (Figure 3J). Both *Pard3*$^{f/f}$ and *Pard3*$^{f/f}$*:CaMKIIα-Cre* entered and spent similar amounts of time in the open arms of the EPM (Figures 3E, 3F, and 3I) and outer edge of the OFT (Figures 3K, 3L, and 3O), indicating no aberrations in anxiety-like behavior. The number of fecal boli at the end of the OFT were also unchanged (Figure S4D). This lack of anxiety-like behaviors further confirms that the enhanced learning and memory observed in the MWM was not conflated by anxiety levels, as spatial learning and memory can be enhanced by increased anxiety-like behavior.[34] Furthermore, there were no differences in the distance traveled or velocity in the EPM (Figures 3G–3H) or OFT (Figures 3M and 3N), suggesting the loss of Par3 does not alter locomotion or exploratory behavior. We also scored behaviors in the OFT, including grooming, supported rearing against the chamber wall, unsupported rearing, and jumping. Interestingly, although loss of Par3 lead to an increase in marble burying behavior, it did not significant change grooming (Figures 3R and S4C), which is also a repetitive behavior. Furthermore, we observed a small but significant decrease in the time spent in supported rearing (Figure 3P, $p = 0.0462$) but not unsupported rearing (Figures 3Q and S4B) or number of supported rearing (Figure S4A). *Pard3*$^{f/f}$*:CaMKIIα-Cre* mice also showed a trend toward increased repetitive jumping in the OFT (Figure 3S), consistent with what we observed in the MWM test (Figure 3A).

Finally, we examined whether forebrain loss of Par3 affects the social behaviors of mice. Mice were subjected to the three-chamber social interactions test. Mice were allowed to explore the 3 compartments containing two identical wire mesh cups in opposite corners for 10 min during a habituation trial (Figures S4E–S4I). 24 h later, sociability was tested. Mice were allowed 10 min to explore and interact with an age- and sex-matched stranger mouse placed in one of the wire mesh cups. Both *Pard3*$^{f/f}$ and *Pard3*$^{f/f}$*:CaMKIIα-Cre* spent significantly more time in the compartment containing the stranger mouse compared to the compartment containing the empty cup (Figure 3T, *Pard3*$^{f/f}$: $p = 0.0011$ and *Pard3*$^{f/f}$*:CaMKIIα-Cre*: $p = 0.0246$) and more time interacting with the cup containing the stranger mouse versus the empty cup (Figure 3U, *Pard3*$^{f/f}$: $p = 0.0002$ and *Pard3*$^{f/f}$*:CaMKIIα-Cre*: $p = 0.0031$). No significant genotype difference was observed in the preference index for time spent in the compartment containing the stranger (Figure 3V) or the preference index for the time spent interacting with the cup containing the stranger mouse (Figures 3W and 3X). Together, these data demonstrate the forebrain loss of Par3 enhances repetitive behaviors like jumping and marble burying without altering anxiety-like behavior, locomotion, or social interactions.

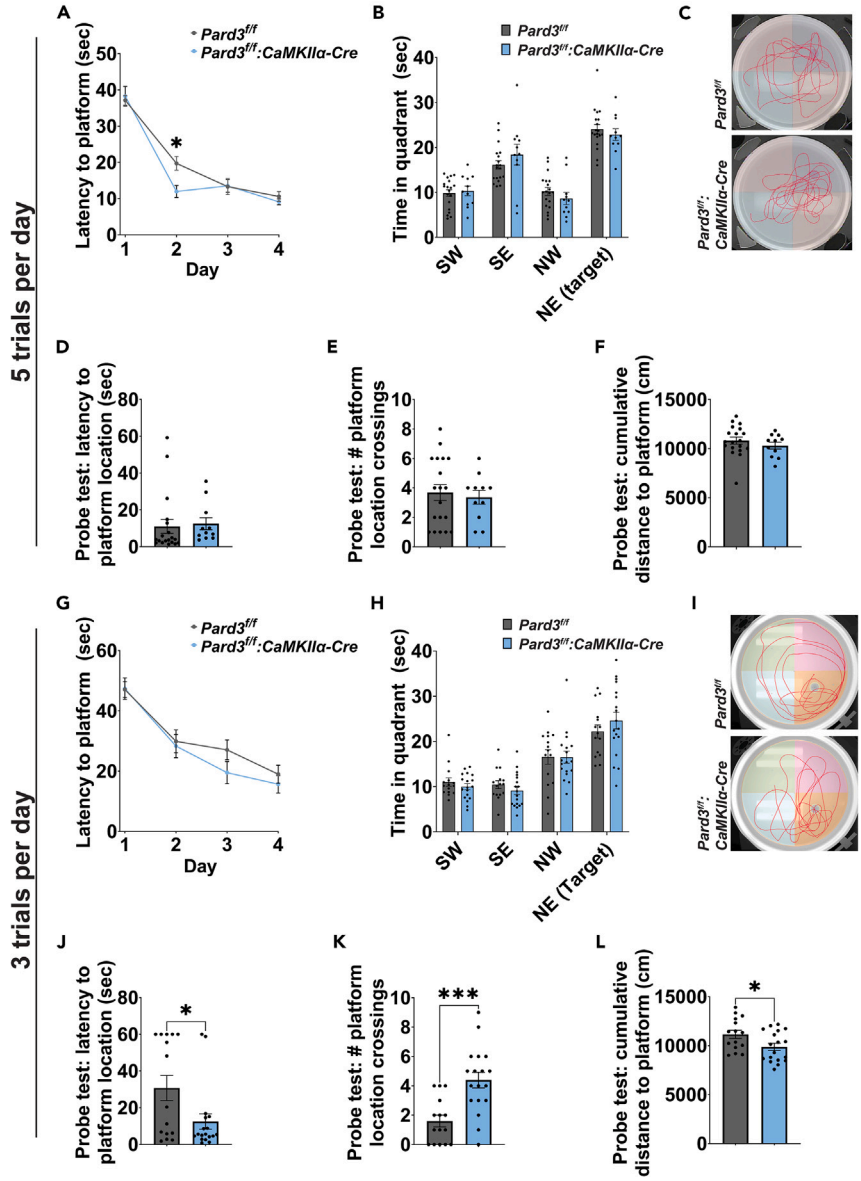

Figure 2. Enhanced spatial learning and memory in the *Pard3$^{f/f}$:CaMKIIα-Cre* mice

(A) Latency to reach the platform in seconds by day with 5 trials per day. Data represented by mean ± SEM, analyzed via two-way ANOVA with Sidak's multiple comparisons test. *$p \leq 0.05$.

(B) Time spent in each quadrant during the 60 s probe test during which the platform was removed from the NE target quadrant. Data representation includes individual mice as points and bar graphs as mean ± SEM, analyzed with two-way ANOVA with Sidak's multiple comparisons test.

(C) Representative swim paths during probe test.

(D–F) Quantification during probe test including (D) latency to prior platform location, (E) number of platform location crossings, and (F) cumulative distance to prior platform location. Data representation includes individual mice as points and bar graphs as mean ± SEM, analyzed via unpaired t-test. In (A-F) $N = 11$ male *Pard3$^{f/f}$* mice, 5 male *Pard3$^{f/f}$:CaMKIIα-Cre* mice, 8 female *Pard3$^{f/f}$* mice, 6 female *Pard3$^{f/f}$:CaMKIIα-Cre* mice.

(G) Latency to reach the platform in seconds by day with 3 trials per day. Data represented by mean ± SEM, analyzed via two-way ANOVA with Sidak's multiple comparisons test.

(H) Time spent in each quadrant during the 60-s probe test during which the platform was removed from the NE target quadrant. Data representation includes individual mice as points and bar graphs as mean ± SEM, analyzed with two-way ANOVA with Tukey's multiple comparison test.

(I) Representative swim paths during probe test.

(J–L) Quantification during probe test including (J) latency to prior platform location, (K) number of platform location crossings, and (L) cumulative distance to prior platform location. Data representation includes individual mice as points and bar graphs as mean ± SEM, analyzed via unpaired t-test. *$p \leq 0.05$, ***$p \leq 0.001$. In (G-L) $N = 10$ male *Pard3$^{f/f}$* mice, 8 male *Pard3$^{f/f}$:CaMKIIα-Cre* mice, 5 female *Pard3$^{f/f}$* mice, 10 female *Pard3$^{f/f}$:CaMKIIα-Cre* mice.

See also Figure S3.

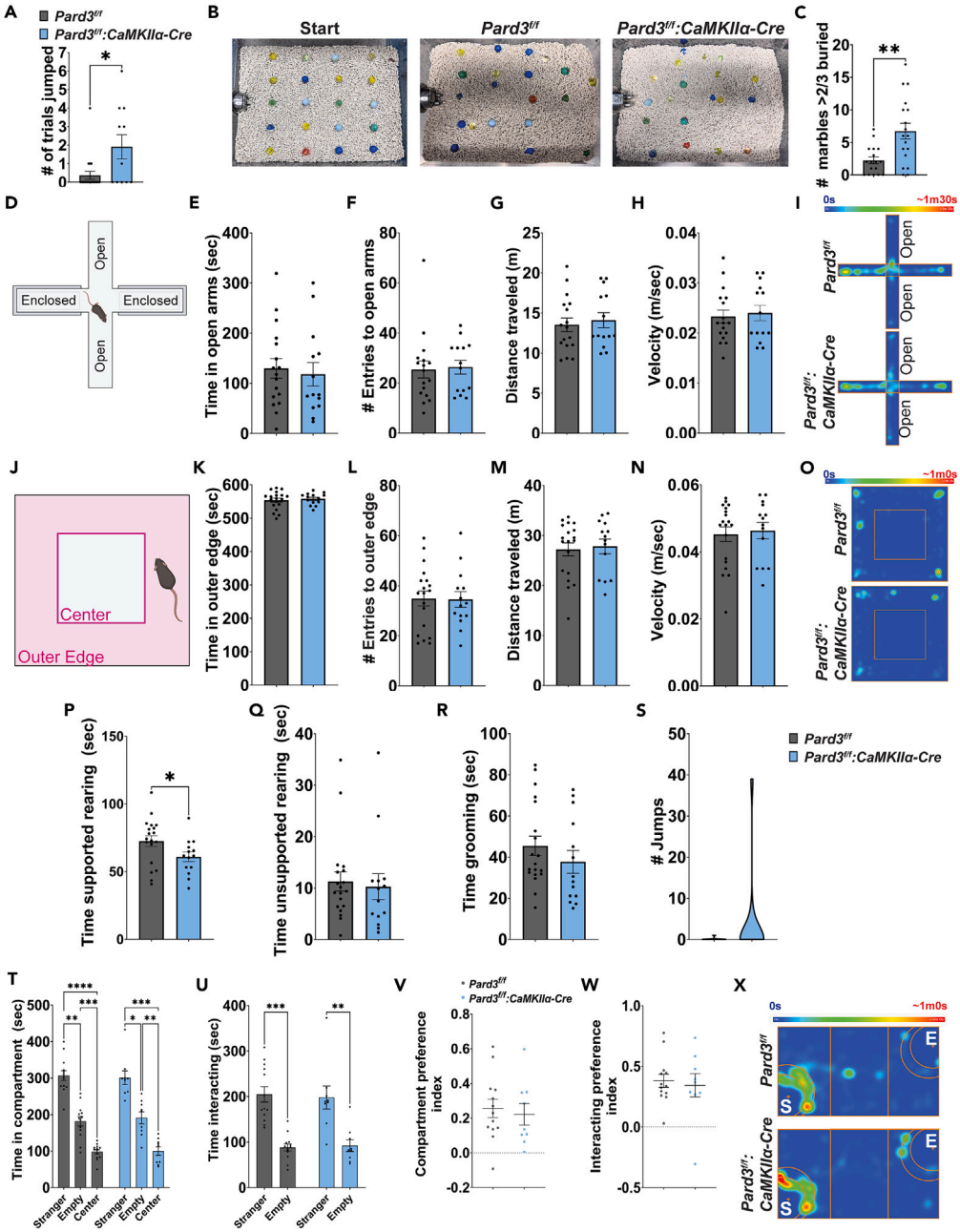

Figure 3. ASD-related behavioral phenotypes in the *Pard3*$^{f/f}$*:CaMKIIα-Cre* mice

(A) Quantification of jumping behavior observed at the conclusion of MWM training trials. *N* = 11 male *Pard3*$^{f/f}$ mice, 5 male *Pard3*$^{f/f}$*:CaMKIIα-Cre* mice, 8 female *Pard3*$^{f/f}$ mice, 6 female *Pard3*$^{f/f}$*:CaMKIIα-Cre* mice. Data represented by individual mice as points and bar graphs as mean ± SEM, analyzed with unpaired t-test. *$p \leq 0.05$.

(B) Representative images for starting position and final location of marbles buried.

(C) Quantification of marbles buried by > 2/3. *N* = 8 male *Pard3*$^{f/f}$ mice, 8 male *Pard3*$^{f/f}$*:CaMKIIα-Cre* mice, 5 female *Pard3*$^{f/f}$ mice, 10 female *Pard3*$^{f/f}$*:CaMKIIα-Cre* mice. Data represented by individual mice as points and bar graphs as mean ± SEM, analyzed with unpaired t-test. **$p \leq 0.01$.

(D) Diagram of the EPM apparatus with enclosed and open arms.

(E–H) Quantification during the EPM of (E) time in open arms, (F) number of entries into open arms, (G) total distance traveled, and (H) average velocity. *N* = 6 male *Pard3*$^{f/f}$ mice, 8 male *Pard3*$^{f/f}$*:CaMKIIα-Cre* mice, 11 female *Pard3*$^{f/f}$ mice, 6 female *Pard3*$^{f/f}$*:CaMKIIα-Cre* mice. Data representation includes individual mice as points and bar graphs as mean ± SEM, analyzed with unpaired t-test.

(I) Representative heatmap for EPM.

(J) Diagram of the OFT chamber with outer edge versus center.

Figure 3. *Continued*

(K–R) Quantification during the OFT of (K) time in outer edge, (L) number of entries into outer edge, (M) total distance traveled, (N) average velocity, (P) time supported rearing at chamber wall, (Q) time unsupported rearing, and (R) time grooming. Data representation includes individual mice as points and bar graphs as mean ± SEM, analyzed with unpaired t-test. *$p \leq 0.05$.

(S) Number of jumps. Data representation includes violin plot, analyzed with unpaired t-test. In (K-S) $N = 6$ male *Pard3*$^{f/f}$ mice, 8 male *Pard3*$^{f/f}$:*CaMKIIα-Cre* mice, 13 female *Pard3*$^{f/f}$ mice, 6 female *Pard3*$^{f/f}$:*CaMKIIα-Cre* mice. (O) Representative heatmap for OFT.

(T–W) Quantification of sociability test including (T) time in each compartment, (U) time interacting with stranger cup and empty cup, (V) preference index for stranger versus empty compartment, and (W) preference index for interacting with stranger cup versus empty cup. $N = 6$ male *Pard3*$^{f/f}$ mice, 3 male *Pard3*$^{f/f}$:*CaMKIIα-Cre* mice, 7 female *Pard3*$^{f/f}$ mice, 6 female *Pard3*$^{f/f}$:*CaMKIIα-Cre* mice. (T-U) Data representation includes individual mice as points and bar graphs as mean ± SEM, analyzed via two-way ANOVA with Sidak's or Tukey's multiple comparison test. *$p \leq 0.05$, **$p \leq 0.01$, ***$p \leq 0.001$, ****$p \leq 0.0001$. (V-W) Data representation includes individual mice as points and horizontal bar as mean ± SEM, analyzed via unpaired t-test.

(X) Representative heatmap for sociability test including the stranger cup ("S") and empty cup ("E").

See also Figure S4.

Phosphoproteomics shows dysregulation of cytoskeletal dynamics upon loss of Par3

To explore downstream pathways of Par3, we performed unbiased phosphoproteomics of hippocampal lysates from *Pard3*$^{f/f}$ and *Pard3*$^{f/f}$:*CaMKIIα-Cre* mice. Following phosphopeptide enrichment, samples were analyzed by liquid chromatography with tandem mass spectroscopy (LC-MS/MS). We identified 69 phosphosites on 67 proteins that are significantly dysregulated in the *Pard3*$^{f/f}$:*CaMKIIα-Cre* as compared with littermate *Pard3*$^{f/f}$ control mice (Figures 4A and 4B, Table S1). We then performed gene ontology (GO) analysis in Database for Annotation, Visualization, and Integrated Discovery (DAVID).[35,36] Interestingly, we found that proteins that bind to actin or microtubules and regulate their assembly and function were among the most significantly dysregulated in the Par3 cKO hippocampus (Figures 4C–4E). Phosphorylation of major synaptic scaffolding proteins and glutamate receptors were not significantly altered (Table S2), further confirming the lack of changes in synaptic proteins in the PSD-enriched fraction. These data suggest that loss of Par3 leads to dysregulation of cytoskeletal dynamics in hippocampal pyramidal neurons.

Loss of Par3 activates the Rac-PAK pathway

The observed dysregulation of cytoskeletal proteins concurs with prior studies demonstrating Par3 is upstream of TIAM1 to regulate Rac activation,[13,15,17,37,38] a key regulator of actin and microtubule dynamics. However, most of these studies were completed in non-neuronal cell types or in primary neuronal culture *in vitro* and report conflicting results. To investigate Rac activity *in vivo*, we used a p21-binding domain (PBD) pulldown assay to determine if Rac1 activation is altered in *Pard3*$^{f/f}$:*CaMKIIα-Cre* hippocampal tissue. The PBD domain of the Rac/Cdc42 effector protein p21-activated kinase (PAK) binds GTP-bound Rac or Cdc42, enabling the detection of active Rac1 by western blot. The loss of Par3 results in increased Rac1 activity as indicated by an ~53% increase of active Rac1 pulled down by PAK-PBD (Figures 5A and 5B, $p = 0.0065$). Furthermore, we examined the activation of PAK downstream of Rac1. We found the *Pard3*$^{f/f}$:*CaMKIIα-Cre* hippocampal PSD-enriched fractions have increased phospho-PAK1 (Ser144)/PAK2 (Ser141) and no change in total PAK expression (Figures 5C and 5D, phospho-PAK: $p = 0.0077$, phospho-PAK/total PAK: $p = 0.0074$), indicating an increase in PAK activity.[39] Together, this data suggests Par3 negatively regulates Rac1 and PAK activity in the hippocampus.

Loss of Par3 leads to dysregulated microtubule dynamics through CAMSAP2 phosphorylation

Next, we sought to examine specifically how cytoskeletal dynamics may be affected downstream of Par3. Among the dysregulated proteins identified in the phosphoproteomics, the calmodulin regulated spectrin associated protein (CAMSAP) family is particularly interesting since both CAMSAP2 and CAMSAP3 show significantly upregulated phosphorylation in the *Pard3*$^{f/f}$:*CaMKIIα-Cre* hippocampus (Figure 4A). The CAMSAP family of proteins specifically bind to and stabilize the minus-end of microtubules (MTs).[40] We focused on CAMSAP2 since it is the most abundantly expressed CAMSAP in the hippocampus and is present in dendrites, whereas CAMSAP3 is axonally localized.[41,42] Phosphoproteomics data reveal that serine 992 (S992) of CAMSAP2 was significantly upregulated in the *Pard3*$^{f/f}$:*CaMKIIα-Cre* hippocampus S992 is located in the microtubule binding domain (MBD) of CAMSAP2, which binds to stabilized but not dynamic MTs.[43] Thus, we wondered whether S992 phosphorylation in the MBD affects MT binding. To examine this possibility, we transfected GFP-tagged human CAMSAP2 constructs into primary hippocampal neurons. In human CAMSAP2, the serine residue equivalent to the mouse S992 is S1019. Then, we generated non-phosphorylatable and phosphomimetic mutations for S1019 and examined their interactions with microtubules using fluorescent recovery after photobleaching (FRAP) imaging. We found no significant differences in the fluorescence recovery between GFP-CAMSAP2 WT, S1019A, or S1019D (Figures 6A–6D). This suggests that S1019 phosphorylation does not significantly affect the kinetics of CAMSAP2 and MT binding dynamics.

CAMSAP2 decorates MT minus-ends, which is strongly coupled to the polymerization of MT-minus-ends. Thus, CAMSAP2 decoration length correlates with MT stabilization.[43] We sought to determine whether S1019 phosphorylation on CAMSAP2 changes CAMSAP2 decoration lengths at the MT minus-ends. GFP-CAMSAP2 WT and S1019 mutants were transfected into Rat2 fibroblasts. Cells were imaged live and the stretches of CAMSAP2 decoration on MT were measured. Interestingly, we found the non-phosphorylatable S1019A mutation leads to significantly increased CAMSAP2 decoration length on MT, whereas the phosphomimetic S1019D mutant leads to a significant decrease in the length of CAMSAP2 stretches (Figures 6E and 6F, WT vs. S1019A $p = 0.0010$, WT vs. S1019D $p < 0.0001$, S1019A vs. S1019D $p < 0.0001$).

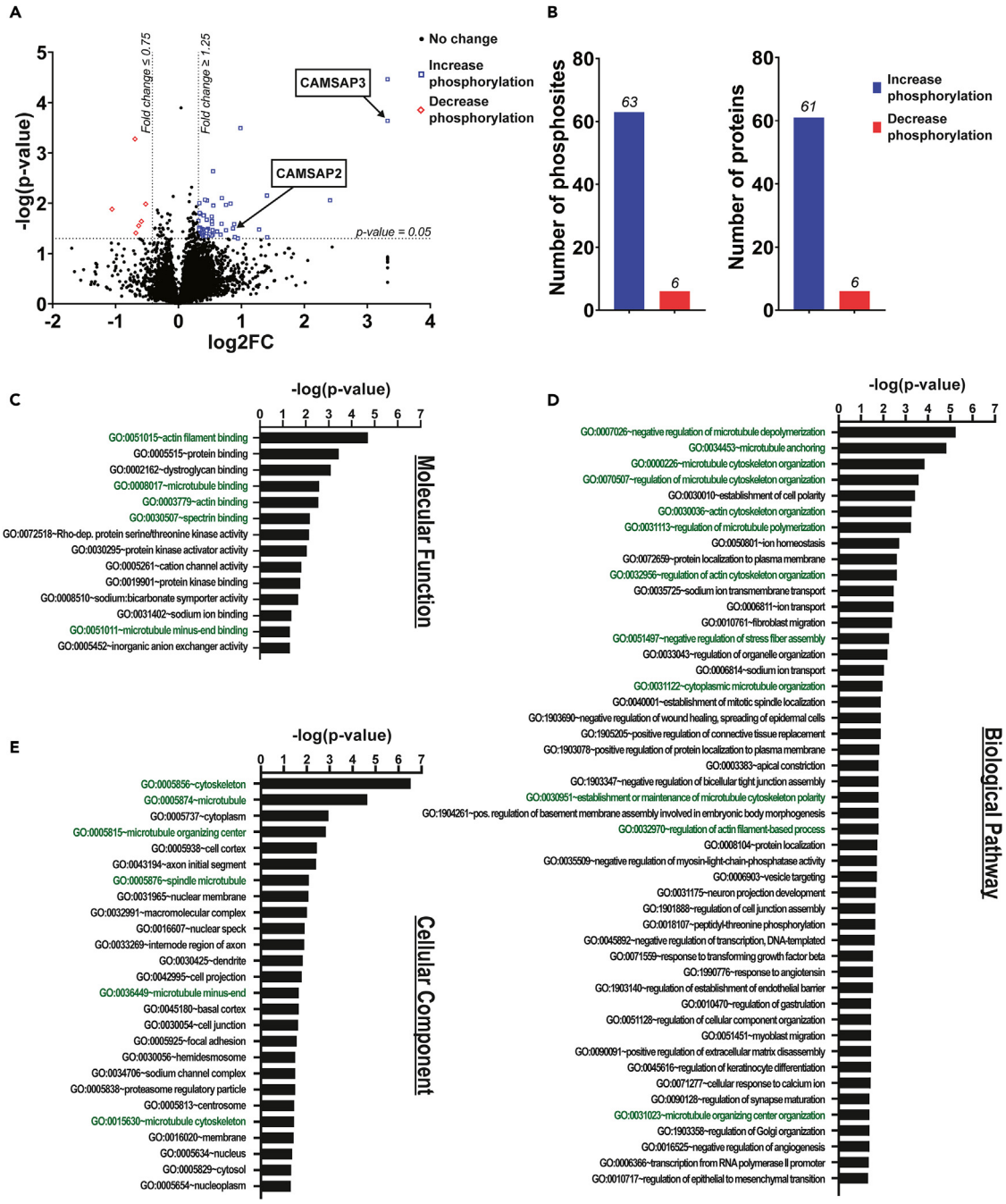

Figure 4. Par3 regulates phosphorylation of cytoskeleton-related proteins

(A) Phosphoproteomic analysis of hippocampal tissue. $N = 3$ *Pard3*$^{f/f}$ mice and 3 *Pard3*$^{f/f}$*:CaMKIIα-Cre* mice, analyzed with unpaired t-test.

(B) Number of phosphosites and proteins with altered phosphorylation states due to the loss of Par3.

(C and D) Associated GO analysis of (C) molecular function, (D) biological pathway, and (E) cellular component of genes altered in phosphoproteomics of *Pard3*$^{f/f}$*:CaMKIIα-Cre* using DAVID. Green GO terms are directly cytoskeleton related.

See also Tables S1 and S2.

Since CAMSAP2 decoration lengths on MT is coupled to MT minus-end growth,[43] these results suggest that CAMSAP2 S1019A interaction with MT promotes MT minus-end growth and stabilization.

We then examined how CAMSAP2 interactions with MT might be altered at the synaptic level in the hippocampus. We isolated PSD-enriched fractions from *Pard3*$^{f/f}$ and *Pard3*$^{f/f}$*:CaMKIIα-Cre* hippocampus as described above and determined the levels of CAMSAP2. We also

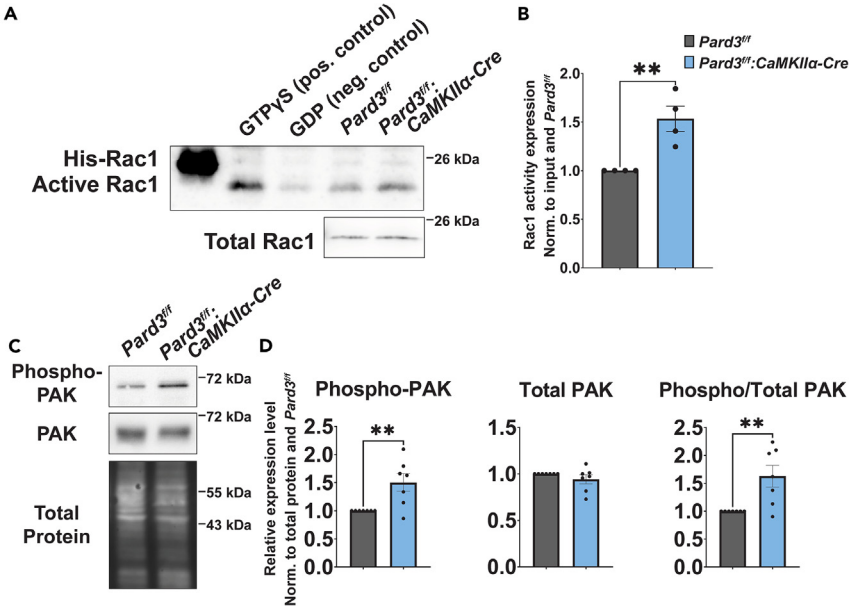

Figure 5. Enhanced activation of the Rac1-PAK pathway in the *Pard3$^{f/f}$:CaMKIIα-Cre* mice

(A) Representative images of Western blots of Rac1 activity assay.

(B) Quantification of Rac1 activity in hippocampal tissue normalized to total Rac1 and *Pard3$^{f/f}$*. $N = 4$ *Pard3$^{f/f}$* mice and 4 *Pard3$^{f/f}$:CaMKIIα-Cre* mice. Data representation includes individual mice as points and bar graphs as mean ± SEM, analyzed with unpaired t-test. $^{**}p \leq 0.01$.

(C) Representative images for phospho- and total PAK detected from PSD-enriched fractions derived from hippocampal tissue.

(D) Quantification of relative protein expression levels normalized to total protein and *Pard3$^{f/f}$* for phosphorylated PAK, total PAK, and phosphorylated PAK normalized to total PAK. $N = 7$ *Pard3$^{f/f}$* mice and 7 *Pard3$^{f/f}$:CaMKIIα-Cre* mice. Data representation includes individual mice as points and bar graphs as mean ± SEM, analyzed with unpaired t-test. $^{**}p \leq 0.01$.

determined the levels of α-tubulin and acetylated tubulin (ace-tubulin), which represent total and stable microtubules respectively. Interestingly, we observed a significant decrease in the level of CAMSAP2 in the PSD-enriched fraction (Figures 6G and 6H, $p = 0.0004$). Paradoxically, there was a significant increase in the level of ace-tubulin when normalized to total α-tubulin (Figures 6G and 6H, $p = 0.0227$), indicating an increase in the fraction of stable MTs associated with the PSD-enriched fraction. To further explore these changes in CAMSAP2 and MT dynamics, we performed co-immunoprecipitation from *Pard3$^{f/f}$* and *Pard3$^{f/f}$:CaMKIIα-Cre* hippocampal lysates between CAMSAP2 and tubulin. We found in the *Pard3$^{f/f}$:CaMKIIα-Cre* hippocampus a substantial reduction in the amount of both α-tubulin and ace-tubulin associated with CAMSAP2 (Figure 6I). This is consistent with the observation that CAMSAP2 S1019D mutant show significantly reduced MT decoration length. Taken together, our results show the loss of Par3 increases CAMSAP2 S992 phosphorylation altering MT stability at the synapse.

DISCUSSION

In this study, we established a novel forebrain-specific Par3 conditional knockout mouse model to examine the role of Par3 in dendritic spine morphogenesis and cognitive functions *in vivo*. Par3 is a key polarity regulator important for subcellular compartmentalization in several different contexts.[44] Since dendritic spines are highly compartmentalized structures,[9–11,45–48] we predicted the loss of Par3 *in vivo* would cause significant defects in the formation of mature dendritic spines, similar to the loss of mature dendritic spines in Par3 shRNA-expressing primary hippocampal neurons.[15] Unexpectedly, we observed a significant increase in dendritic spine density in the hippocampal CA1 region. The formation of mature, mushroom-shaped dendritic spines was not significantly affected. Instead, the loss of Par3 created an excess pool of long, thin dendritic spines. Consistent with the increased immature-appearing spines, we detected a significant reduction in mEPSC amplitude, suggesting a decrease in synaptic strength in the absence of Par3. These immature-appearing dendritic spines are abundant in the developing brain but are present at a lower density in adult brains. These findings suggest Par3 may serve as a molecular gatekeeper or checkpoint to limit the number of immature dendritic spines. The loss of Par3 may remove the brake on spine formation, leading to dendritic spine neoteny characterized by higher spine density and a larger pool of dendritic spines of immature morphology. However, it is also possible that the increase in immature dendritic spines is due to a lack of synaptic pruning, leaving an abnormally high number of immature spines. In addition, the timing of Par3 ablation likely play a role in the observed spine phenotype. *CaMKIIα-Cre* starts expressing in the third postnatal week,[29] after the initiation of spinogenesis in mice. This may contribute the difference in phenotypes observed *in vitro* and *in vivo*.

The plasticity and stability of dendritic spines is vital to learning and memory processes.[7,49,50] Immature dendritic spines have been proposed as "learning spines". These spines are more dynamic and can undergo potentiation during learning to encode new memories.[51] A finite number of these learning spines may be a rate-limiting step in learning and memory. Interestingly, *Pard3$^{f/f}$:CaMKIIα-Cre* mice

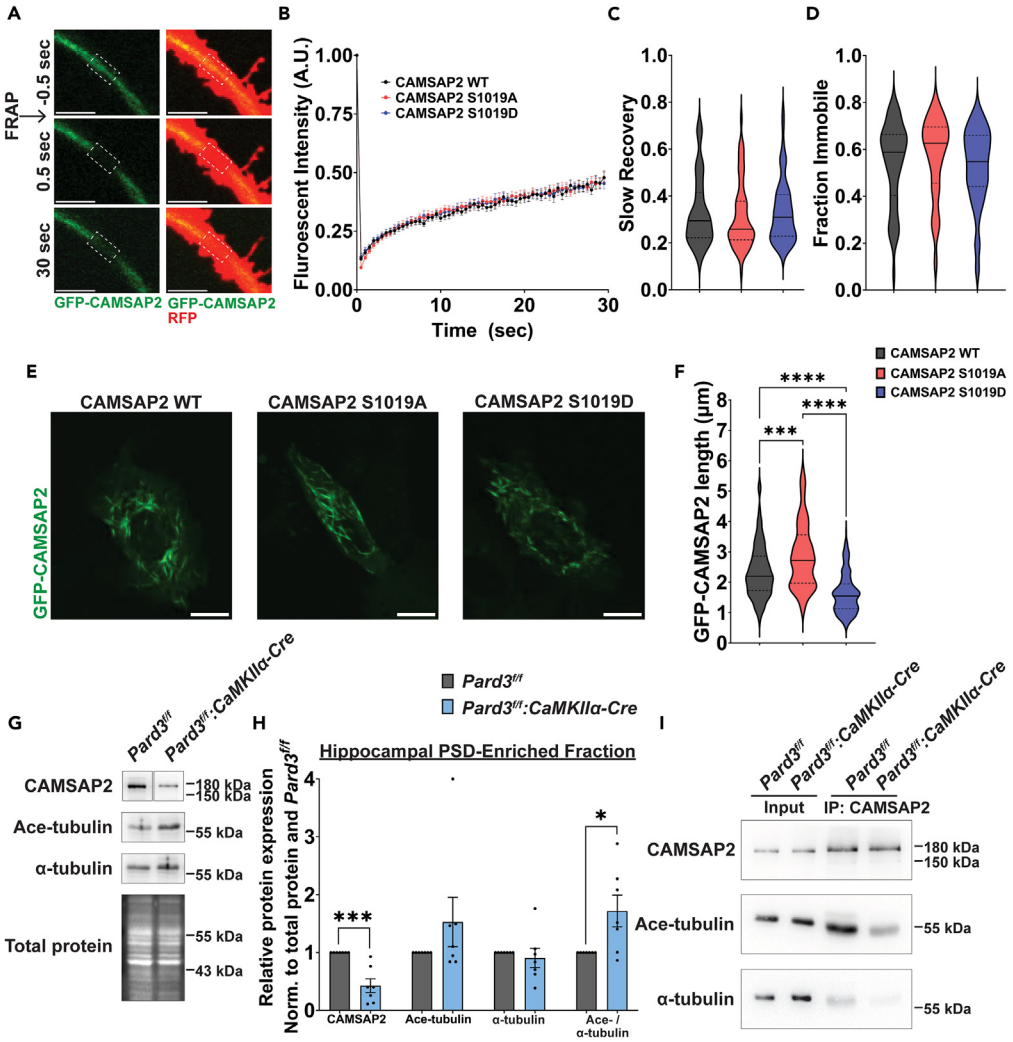

Figure 6. Par3 regulates CAMSAP2 S992 phosphorylation and microtubule dynamics

(A) Representative images of FRAP for GFP-CAMSAP2 WT (green) and RFP (red). Dashed box indicates bleached region. Scale bar = 5μm.

(B) Recovery curve for FRAP. Data representation includes mean ± SEM.

(C) Slow recovery of FRAP recovery curve.

(D) Fraction immobile of FRAP recovery curve. In (C-D), data representation includes violin plots with thick lines as medians and dotted lines as quartiles. $N = 53$ measurements from 20 GFP-CAMSAP2 WT cells, 62 measurements from 23 GFP-CAMSAP2 S1019A cells, and 62 measurements from 24 GFP-CAMSAP2 S1019D cells, analyzed via mixed model analysis.

(E) Representative images of GFP-CAMSAP2 lengths (green) in Rat2 cells. Scale bar = 10μm.

(F) Quantification of GFP-CAMSAP2 lengths in Rat2 cells. $N = 245$ measurements from 8 GFP-CAMSAP2 WT cells, 166 measurements from 10 GFP-CAMSAP2 S1019A cells, and 273 measurements from 15 GFP-CAMSAP2 S1019D cells, analyzed via mixed model analysis. ***$p \leq 0.001$, ****$p \leq 0.0001$.

(G) Representative images of Western blots for CAMSAP2, acetylated (ace) tubulin and α-tubulin detected from PSD-enriched fractions derived from hippocampal tissue.

(H) Quantification of relative protein levels normalized to total protein and *Pard3*$^{f/f}$ for CAMSAP2, ace-tubulin, α-tubulin, and ace-tubulin normalized to α-tubulin. $N = 7$ *Pard3*$^{f/f}$ mice and 7 *Pard3*$^{f/f}$*:CaMKIIα-Cre* mice. Data representation includes individual mice as points and bar graphs as mean ± SEM, analyzed with unpaired t-test. *$p \leq 0.05$, ***$p \leq 0.001$.

(I) Co-immunoprecipitation of CAMSAP2 with ace-tubulin and α-tubulin in hippocampal lysates from *Pard3*$^{f/f}$ and *Pard3*$^{f/f}$*:CaMKIIα-Cre* mice.

exhibited enhanced learning and memory in the MWM. This suggests that the increase in immature-appearing spines facilitates learning by providing a larger pool of spines capable of undergoing potentiation and thereby bypassing a rate-limiting step in learning. Notably, in patients and mouse models of neurodevelopmental disorders including Fragile X syndrome and Rett syndrome, an increase in or shift toward immature dendritic spines is often observed. This is associated with a reduction in mature dendritic spines, leading to learning impairments.[52–58] By contrast, *Pard3*$^{f/f}$*:CaMKIIα-Cre* mice do not show a significant reduction in mature spines and do exhibit enhanced learning

and memory. Thus, it is likely that the loss of Par3 leads to an excess pool of immature spines without impairing the transition from immature to mature spines as evident by the enhanced learning and memory abilities.

Additionally, we demonstrate that the *in vivo* depletion of Par3 leads to an elevation in the activity of the Rac1-PAK pathway. This is consistent with the observation that actin regulators such as Ablim2, Ermin, ROCK1/2, DMTN, Plectin, which are all involved in the RhoA and Rac1 signaling pathways,[59–63] are significantly dysregulated in the phosphoproteomic analysis of *Pard3$^{f/f}$:CaMKIIα-Cre* hippocampus. In addition, previous studies show overexpression of PAK results in increased dendritic spines and synapses in primary hippocampal neurons.[64] Conversely, conditional ablation of Rac1 in forebrain excitatory neurons leads to reduced synaptic density, larger spine heads, and impaired spatial learning.[65] Interestingly, a *de novo* missense mutation in *RAC1* is linked to severe intellectual disability,[66] and *PAK1* and *PAK3* mutations are also known to be associated with intellectual disability,[67–75] indicating a key role for this pathway in higher cognition in humans. Furthermore, Rac activation has been implicated in the high cognitive abilities in humans. Previous studies show the human-specific gene duplication of Slit-Robo Rho-GTPase activating protein 2 (*SRGAP2*) produces SRGAP2C, which inhibits the function of the ancestral SRGAP2A, a GTPase-activating protein (GAP) for Rac1. Thus, the presence of the human specific SRGAP2C will increase Rac1 activation. Expression of SRGAP2C in mice increases dendritic spine density, increases spine length, and enhances cognition,[76,77] which are reminiscent of the *Pard3$^{f/f}$:CaMKIIα-Cre* mice. Considering that SNPs of Par3 have been linked to intelligence and math abilities,[21,22] it would be interesting to explore the effects of these SNPs on Par3 expression and function, and how downstream Rac1 activation may be affected.

Intriguingly, the Rac1 pathway has been linked to forgetting in both *Drosophila* and mammals. In *Drosophila* mushroom body neurons, expression of a constitutively active Rac1 accelerates memory decay whereas a dominant negative Rac1 slows memory decay.[78] Similarly, inhibition of Rac1 activity in the hippocampus impairs the forgetting of contextual fear memory in rats[79] and object recognition memory in mice.[80] Additionally, photoactivation of Rac1 shrinks dendritic spines and erases memory.[7] These studies appear to be at odds with the literature suggesting elevated Rac1 activity in enhanced cognition discussed above. However, it is not surprising considering that both constitutively active and dominant negative Rac1 impairs synapse formation.[81] Thus, precise spatiotemporal regulation of Rac1 activation and inactivation is likely necessary to coordinate learning, memory, and forgetting. Interestingly, Scribble, a basolateral cell polarity determinant, organizes a signalosome involving Rac1 in active forgetting in *Drosophila*.[82] As the Scribble and Par complex play antagonistic roles in apical-basal polarity establishment in epithelial cells,[83] it will be interesting to explore how Scribble and the Par complex coordinate with each other to spatiotemporally regulate Rac activity in learning, memory, and forgetting.

How does Par3 regulate Rac1 activation in dendritic spines *in vivo*? Our previous studies in primary hippocampal neurons demonstrate Par3 restricts Rac1 activity to dendritic spines through interactions with the Rac guanine nucleotide exchange factor TIAM1. Loss of Par3 disperses TIAM1 and active Rac1, leading to a shift to immature dendritic spines.[15] Interestingly, TIAM1 also binds the calcium-calmodulin protein kinase II (CaMKII). After dendritic spine stimulation, CaMKII directly binds to and releases TIAM1 from an autoinhibition state, consequently activating Rac1.[84,85] In future studies, exploring the impact of Par3 regulation on CaMKII-TIAM1 interactions during synaptic plasticity may yield fascinating insights, especially since global deletion of TIAM1 has been shown to enhance contextual fear memory and context discrimination.[86] Finally, in addition to Rac1 activation, other mechanisms may also be at play downstream of the loss of Par3, as we have shown for CAMSAP2 and MT dynamics. Our phosphoproteomics dataset will serve as an important tool for future studies aimed at understanding the signaling mechanisms of the Par polarity complex in dendritic spine plasticity as well as in other cellular processes.

In addition to the Rac1 pathway, we also observed a significant increase in the phosphorylation of CAMSAP proteins in the *Pard3$^{f/f}$:CaMKIIα-Cre* hippocampus. Specifically, we found that CAMSAP2 phosphorylation on S992 (S1019 in human CAMSAP2) regulates its association with the MT minus-end, leading to a reduction in the decoration length of CAMSAP2 on the minus-end. This is consistent with the observed reduction of both α-tubulin and acetylated tubulin associated with CAMSAP2 in the *Pard3$^{f/f}$:CaMKIIα-Cre* hippocampus. In the PSD-enriched fraction of the *Pard3$^{f/f}$:CaMKIIα-Cre* hippocampus, there was a significant increase in the fraction of acetylated tubulin, indicating an increase in stable MT in this fraction. This is consistent with previous studies showing that MT stabilization increases dendritic spine formation while decreased MT stability reduces dendritic spines.[87] Interestingly, in the PSD-enriched fraction, we observed a significant decrease in the level of CAMSAP2. While this appears to be paradoxical with the increased fraction of stable MT, one possible explanation is that MT polarity is altered in the absence of Par3 in the synaptic region. MT plus-ends are known to dynamically enter dendritic spines in an activity-dependent manner.[88,89] However the relationship between MT minus-ends and dendritic spines or dendritic shaft synapses have not been explored. CAMSAP3/Nezha has previously been shown to anchor MT minus-ends to cadherin-mediated zonula adherens in epithelial cells.[90] In the *Drosophila* oocytes, Patronin, a fly homolog of CAMSAPs, anchors MT minus-ends to the anterior cortical actin through Shot, the *Drosophila* spectraplakin. Interestingly, this polarized distribution of Patronin/Shot is regulated by another polarity protein Par1.[91] In the future, it will be interesting to examine whether and how MT minus-ends may be anchored along the dendrites and in or near the synapses and how CAMSAP2 might be involved in this process.

Previous studies have shown MT dynamics and stability are important for learning and memory. Tyrosinated tubulin, representing dynamic MTs, peaks 30 min after learning, while detyrosinated tubulin, a marker for stable MTs, peaks 8 h after contextual fear conditioning learning. Pharmacologically hyperstabilizing MTs 8 h after learning enhances memory retention 24 h after learning, while destabilizing MTs disrupted memory retention.[92] Similarly, destabilization of MTs with nocodazole reduced dendritic spine density and impaired contextual fear memory, which was reversed with the MT-stabilizing Taxol.[93] The effect of MT stabilization is highly time sensitive, as Taxol treatment 30 min after learning reduced memory formation, consistent with the observed increase in MT dynamics during this time frame.[92] Whether and how MT minus-end dynamics and stability are involved in the learning and memory process warrant further investigation.

How does Par3 regulate CAMSAP2 and MT dynamics? A recent study show that synthetic clustering of the Par complex is sufficient to induce cytoskeletal asymmetry.[94] Interestingly, Par complex clustering leads to asymmetrical MT spindles with CAMSAP2 distributed away from the cluster.[94] However, the mechanism for this CAMSAP2 distribution is unknown. Our results suggest that phosphorylation of CAMSAP2 reduces the length of MT minus-end decoration. This is interesting considering that CAMSAP2 is more concentrated on MT in regions away from the Par complex.[94] It would be interesting to examine whether the asymmetric MT spindle distribution observed after Par complex clustering is also associated with differential phosphorylation of CAMSAP2. In the future, it will be important to determine the mechanism by which CAMSAP2 phosphorylation is regulated and how Par3 contributes to this regulation especially during synaptic activation and plasticity as well as in learning and memory processes.

Finally, in addition to enhanced spatial learning and memory, we also observed a significant increase in repetitive behaviors including jumping and marble burying in the *Pard3*$^{f/f}$*:CaMKIIα-Cre* mice. This is interesting as the Par3 family proteins are associated with ASD[19,23–27] and repetitive behavior is a core symptom of ASD. Interestingly, *de novo RAC1* missense mutations have been identified in patients with neurodevelopmental disorders showing stereotypical movements[95,96] and a *de novo* missense variant of *PAK1* causes severe regressive autism.[74] Intriguingly, other ASD-associated behaviors such as social interactions and anxiety-like behaviors are not altered in the *Pard3*$^{f/f}$*:CaMKIIα-Cre* mice. It will be interesting to determine whether loss of Par3 in other brain regions are involved in social or anxiety-like behaviors and the downstream signaling pathways involved in these ASD-related behaviors.

In summary, we established a novel mouse model to conditionally knock out the polarity protein Par3 in forebrain excitatory neurons. Our findings indicate that Par3 acts as a molecular checkpoint to limit immature dendritic spine density *in vivo*. The loss of Par3 leads to dendritic spine neoteny, higher spine density, increased Rac1-PAK activity, and changes in MT dynamics, potentially bypassing a rate-limiting step to enable enhanced learning and memory through increasing the pool of immature spines.

Limitations of the study

In this study, we observed an increase in dendritic spine density in the *Pard3*$^{f/f}$*:CaMKIIα-Cre* mice using Golgi staining. However, Golgi staining cannot inform the dynamics of dendritic spines, and it remains unclear whether the excess pool of dendritic spines result from increased spine formation or a reduction in spine pruning. Future *in vivo* imaging studies on dendritic spine dynamics will be able to shed light on this question. In addition, although we observed increased repetitive behaviors like jumping and marble burying, we did not observe changes in the level of self-grooming in *Pard3*$^{f/f}$*:CaMKIIα-Cre* mice. However, grooming was scored in the open field test, which may be anxiety-inducing. It will be interesting to examine repetitive behaviors like grooming in their home cage environment. Finally, although our studies point to changes in Rac activation and microtubule stability, the use of biochemical fractionation limits our mechanistic understanding of how CAMSAP2 may regulate dendritic spine plasticity. This warrants further investigation using live cell imaging experiments.

STAR★METHODS

Detailed methods are provided in the online version of this paper and include the following:

- KEY RESOURCES TABLE
- RESOURCE AVAILABILITY
  - Lead contact
  - Materials availability
  - Data and code availability
- EXPERIMENTAL MODEL AND STUDY PARTICIPANT DETAILS
  - Generation and genotyping of Pard3 conditional knockout line
- METHOD DETAILS
  - Immunohistochemistry
  - Golgi staining, imaging, and analysis
  - Behavior
  - Primary neuronal culture and fluorescent recovery after photobleaching (FRAP) imaging
  - Cell culture and CAMSAP2 length quantification
  - Synaptosomal fractionation
  - Rac activity assay
  - Co-immunoprecipitation
  - Western blot
  - Electrophysiology
  - Phosphoproteomic analysis
- QUANTIFICATION AND STATISTICAL ANALYSIS

SUPPLEMENTAL INFORMATION

Supplemental information can be found online at https://doi.org/10.1016/j.isci.2024.110308.

ACKNOWLEDGMENTS

The authors would like to thank Drs. David Barker, David Crockett, Bonnie Firestein, Christopher Rongo, and Loren Runnels for feedback on experimental design and manuscript. The authors would also like to thank Dr. Janet Alder for use of her MWM, Dr. Kiran Madura for the use of his microscope, and Dr. Michael Matise, Dr. Ian Macara, and Dr. Zhaohui Feng for reagents. The authors would like to thank Dr. Haiyan Zheng at the Biological Mass Spectrometry Facility at Rutgers University for completing the phosphoproteomic measurements and analysis. Cartoon diagrams and graphical abstract were created with BioRender. This work was supported by NIH grants F31NS122477 to M.M.V., R01NS089578 and R21NS125782 to H.Z., and S10OD025140 to the Rutgers Biological Mass Spectrometry Facility.

AUTHOR CONTRIBUTIONS

Conceptualization, M.M.V., Z.P.P., and H.Z.; Methodology, M.M.V. and M.S.; Formal Analysis, M.M.V. and M.B.; Investigation, M.M.V., E.N.O., N.I., M.B., R.T., and M.S.; Writing – Original Draft, M.M.V. and H.Z.; Writing – Review and Editing, M.M.V., E.N.O., N.I., M.B., R.T., M.S., Z.P.P., and H.Z.; Funding Acquisition, M.M.V. and H.Z.; Supervision, Z.P.P. and H.Z.

DECLARATION OF INTERESTS

The authors declare no competing interests.

Received: September 12, 2023
Revised: March 25, 2024
Accepted: June 17, 2024
Published: June 19, 2024

REFERENCES

1. Bailey, C.H., and Kandel, E.R. (1993). Structural Changes Accompanying Memory Storage. Annu. Rev. Physiol. *55*, 397–426. https://doi.org/10.1146/annurev.ph.55.030193.002145.
2. Huang, L., Zhou, H., Chen, K., Chen, X., and Yang, G. (2020). Learning-Dependent Dendritic Spine Plasticity Is Reduced in the Aged Mouse Cortex. Front. Neural Circuits *14*, 581435. https://doi.org/10.3389/fncir.2020.581435.
3. Hofer, S.B., Mrsic-Flogel, T.D., Bonhoeffer, T., and Hübener, M. (2009). Experience leaves a lasting structural trace in cortical circuits. Nature *457*, 313–317. https://doi.org/10.1038/nature07487.
4. Xu, T., Yu, X., Perlik, A.J., Tobin, W.F., Zweig, J.A., Tennant, K., Jones, T., and Zuo, Y. (2009). Rapid formation and selective stabilization of synapses for enduring motor memories. Nature *462*, 915–919.
5. Kim, S.K., and Nabekura, J. (2011). Rapid synaptic remodeling in the adult somatosensory cortex following peripheral nerve injury and its association with neuropathic pain. J. Neurosci. *31*, 5477–5482. https://doi.org/10.1523/jneurosci.0328-11.2011.
6. Lai, C.S.W., Franke, T.F., and Gan, W.B. (2012). Opposite effects of fear conditioning and extinction on dendritic spine remodelling. Nature *483*, 87–91. https://doi.org/10.1038/nature10792.
7. Hayashi-Takagi, A., Yagishita, S., Nakamura, M., Shirai, F., Wu, Y.I., Loshbaugh, A.L., Kuhlman, B., Hahn, K.M., and Kasai, H. (2015). Labelling and optical erasure of synaptic memory traces in the motor cortex. Nature *525*, 333–338. https://doi.org/10.1038/nature15257.
8. Yang, G., Pan, F., and Gan, W.-B. (2009). Stably maintained dendritic spines are associated with lifelong memories. Nature *462*, 920–924. https://doi.org/10.1038/nature08577.
9. Colgan, L.A., and Yasuda, R. (2014). Plasticity of dendritic spines: subcompartmentalization of signaling. Annu. Rev. Physiol. *76*, 365–385. https://doi.org/10.1146/annurev-physiol-021113-170400.
10. Hotulainen, P., and Hoogenraad, C.C. (2010). Actin in dendritic spines: connecting dynamics to function. J. Cell Biol. *189*, 619–629. https://doi.org/10.1083/jcb.201003008.
11. Spence, E.F., and Soderling, S.H. (2015). Actin Out: Regulation of the Synaptic Cytoskeleton. J. Biol. Chem. *290*, 28613–28622. https://doi.org/10.1074/jbc.R115.655118.
12. Rodriguez-Boulan, E., and Macara, I.G. (2014). Organization and execution of the epithelial polarity programme. Nat. Rev. Mol. Cell Biol. *15*, 225–242. https://doi.org/10.1038/nrm3775.
13. Landin Malt, A., Dailey, Z., Holbrook-Rasmussen, J., Zheng, Y., Hogan, A., Du, Q., and Lu, X. (2019). Par3 is essential for the establishment of planar cell polarity of inner ear hair cells. Proc. Natl. Acad. Sci. USA *116*, 4999–5008. https://doi.org/10.1073/pnas.1816333116.
14. Chuykin, I., Ossipova, O., and Sokol, S.Y. (2018). Par3 interacts with Prickle3 to generate apical PCP complexes in the vertebrate neural plate. Elife *7*, e37881. https://doi.org/10.7554/eLife.37881.
15. Zhang, H., and Macara, I.G. (2006). The polarity protein PAR-3 and TIAM1 cooperate in dendritic spine morphogenesis. Nat. Cell Biol. *8*, 227–237.
16. Zhang, H., and Macara, I.G. (2008). The PAR-6 polarity protein regulates dendritic spine morphogenesis through p190 RhoGAP and the Rho GTPase. Dev. Cell *14*, 216–226.
17. Duman, J.G., Tzeng, C.P., Tu, Y.-K., Munjal, T., Schwechter, B., Ho, T.S.-Y., and Tolias, K.F. (2013). The adhesion-GPCR BAI1 regulates synaptogenesis by controlling the recruitment of the Par3/Tiam1 polarity complex to synaptic sites. J. Neurosci. *33*, 6964–6978. https://doi.org/10.1523/JNEUROSCI.3978-12.2013.
18. Scott, J., Thakar, S., Mao, Y., Qin, H., Hejran, H., Lee, S.Y., Yu, T., Klezovitch, O., Cheng, H., Mu, Y., et al. (2019). Apical-Basal Polarity Signaling Components, Lgl1 and aPKCs, Control Glutamatergic Synapse Number and Function. iScience *20*, 25–41. https://doi.org/10.1016/j.isci.2019.09.005.
19. Pinto, D., Delaby, E., Merico, D., Barbosa, M., Merikangas, A., Klei, L., Thiruvahindrapuram, B., Xu, X., Ziman, R., Wang, Z., et al. (2014). Convergence of Genes and Cellular Pathways Dysregulated in Autism Spectrum Disorders. Am. J. Hum. Genet. *94*, 677–694. https://doi.org/10.1016/j.ajhg.2014.03.018.
20. Kim, S.K., Lee, J.Y., Park, H.J., Kim, J.W., and Chung, J.-H. (2012). Association study between polymorphisms of the PARD3 gene and schizophrenia. Exp. Ther. Med. *3*, 881–885. https://doi.org/10.3892/etm.2012.496.
21. Davies, G., Lam, M., Harris, S.E., Trampush, J.W., Luciano, M., Hill, W.D., Hagenaars, S.P., Ritchie, S.J., Marioni, R.E., Fawns-Ritchie, C., et al. (2018). Study of 300,486 individuals identifies 148 independent genetic loci influencing general cognitive function. Nat. Commun. *9*, 2098. https://doi.org/10.1038/s41467-018-04362-x.
22. Lee, J.J., Wedow, R., Okbay, A., Kong, E., Maghzian, O., Zacher, M., Nguyen-Viet, T.A., Bowers, P., Sidorenko, J., Karlsson Linnér, R., et al. (2018). Gene discovery and polygenic prediction from a genome-wide association study of educational attainment in 1.1 million individuals. Nat. Genet. *50*, 1112–1121. https://doi.org/10.1038/s41588-018-0147-3.
23. Wang, T., Guo, H., Xiong, B., Stessman, H.A.F., Wu, H., Coe, B.P., Turner, T.N., Liu, Y., Zhao, W., Hoekzema, K., et al. (2016). De novo genic mutations among a Chinese

autism spectrum disorder cohort. Nat. Commun. *7*, 13316. https://doi.org/10.1038/ncomms13316.

24. Stessman, H.A.F., Xiong, B., Coe, B.P., Wang, T., Hoekzema, K., Fenckova, M., Kvarnung, M., Gerdts, J., Trinh, S., Cosemans, N., et al. (2017). Targeted sequencing identifies 91 neurodevelopmental-disorder risk genes with autism and developmental-disability biases. Nat. Genet. *49*, 515–526. https://doi.org/10.1038/ng.3792.
25. Guo, H., Wang, T., Wu, H., Long, M., Coe, B.P., Li, H., Xun, G., Ou, J., Chen, B., Duan, G., et al. (2018). Inherited and multiple *de novo* mutations in autism/developmental delay risk genes suggest a multifactorial model. Mol. Autism. *9*, 64. https://doi.org/10.1186/s13229-018-0247-z.
26. Zhou, X., Feliciano, P., Shu, C., Wang, T., Astrovskaya, I., Hall, J.B., Obiajulu, J.U., Wright, J.R., Murali, S.C., Xu, S.X., et al. (2022). Integrating *de novo* and inherited variants in 42,607 autism cases identifies mutations in new moderate-risk genes. Nat. Genet. *54*, 1305–1319. https://doi.org/10.1038/s41588-022-01148-2.
27. Anney, R., Klei, L., Pinto, D., Almeida, J., Bacchelli, E., Baird, G., Bolshakova, N., Bölte, S., Bolton, P.F., Bourgeron, T., et al. (2012). Individual common variants exert weak effects on the risk for autism spectrum disorders. Hum. Mol. Genet. *21*, 4781–4792. https://doi.org/10.1093/hmg/dds301.
28. Insolera, R., Chen, S., and Shi, S.H. (2011). Par proteins and neuronal polarity. Dev. Neurobiol. *71*, 483–494. https://doi.org/10.1002/dneu.20867.
29. Tsien, J.Z., Chen, D.F., Gerber, D., Tom, C., Mercer, E.H., Anderson, D.J., Mayford, M., Kandel, E.R., and Tonegawa, S. (1996). Subregion- and cell type-restricted gene knockout in mouse brain. Cell *87*, 1317–1326.
30. Kim, I.H., Wang, H., Soderling, S.H., and Yasuda, R. (2014). Loss of Cdc42 leads to defects in synaptic plasticity and remote memory recall. Elife *3*, e02839. https://doi.org/10.7554/eLife.02839.
31. Shors, T.J., Chua, C., and Falduto, J. (2001). Sex differences and opposite effects of stress on dendritic spine density in the male versus female hippocampus. J. Neurosci. *21*, 6292–6297. https://doi.org/10.1523/jneurosci.21-16-06292.2001.
32. Won, H., Lee, H.-R., Gee, H.Y., Mah, W., Kim, J.-I., Lee, J., Ha, S., Chung, C., Jung, E.S., Cho, Y.S., et al. (2012). Autistic-like social behaviour in Shank2-mutant mice improved by restoring NMDA receptor function. Nature *486*, 261–265. https://doi.org/10.1038/nature11208.
33. Thomas, A., Burant, A., Bui, N., Graham, D., Yuva-Paylor, L.A., and Paylor, R. (2009). Marble burying reflects a repetitive and perseverative behavior more than novelty-induced anxiety. Psychopharmacology (Berl) *204*, 361–373. https://doi.org/10.1007/s00213-009-1466-y.
34. Eysenck, M.W. (1979). Anxiety, learning, and memory: A reconceptualization. J. Res. Pers. *13*, 363–385. https://doi.org/10.1016/0092-6566(79)90001-1.
35. Huang, D.W., Sherman, B.T., and Lempicki, R.A. (2009). Systematic and integrative analysis of large gene lists using DAVID bioinformatics resources. Nat. Protoc. *4*, 44–57. https://doi.org/10.1038/nprot.2008.211.
36. Huang, D.W., Sherman, B.T., and Lempicki, R.A. (2009). Bioinformatics enrichment tools: paths toward the comprehensive functional analysis of large gene lists. Nucleic Acids Res. *37*, 1–13. https://doi.org/10.1093/nar/gkn923.
37. Chen, X., and Macara, I.G. (2005). Par-3 controls tight junction assembly through the Rac exchange factor Tiam1. Nat. Cell Biol. *7*, 262–269.
38. Nishimura, T., Yamaguchi, T., Kato, K., Yoshizawa, M., Nabeshima, Y.I., Ohno, S., Hoshino, M., and Kaibuchi, K. (2005). PAR-6-PAR-3 mediates Cdc42-induced Rac activation through the Rac GEFs STEF/Tiam1. Nat. Cell Biol. *7*, 270–277.
39. Chong, C., Tan, L., Lim, L., and Manser, E. (2001). The mechanism of PAK activation. Autophosphorylation events in both regulatory and kinase domains control activity. J. Biol. Chem. *276*, 17347–17353. https://doi.org/10.1074/jbc.M009316200.
40. Akhmanova, A., and Steinmetz, M.O. (2019). Microtubule minus-end regulation at a glance. J. Cell Sci. *132*, jcs227850. https://doi.org/10.1242/jcs.227850.
41. Yau, K.W., van Beuningen, S.F.B., Cunha-Ferreira, I., Cloin, B.M.C., van Battum, E.Y., Will, L., Schätzle, P., Tas, R.P., van Krugten, J., Katrukha, E.A., et al. (2014). Microtubule minus-end binding protein CAMSAP2 controls axon specification and dendrite development. Neuron *82*, 1058–1073. https://doi.org/10.1016/j.neuron.2014.04.019.
42. Pongrakhananon, V., Saito, H., Hiver, S., Abe, T., Shioi, G., Meng, W., and Takeichi, M. (2018). CAMSAP3 maintains neuronal polarity through regulation of microtubule stability. Proc. Natl. Acad. Sci. USA *115*, 9750–9755. https://doi.org/10.1073/pnas.1803875115.
43. Jiang, K., Hua, S., Mohan, R., Grigoriev, I., Yau, K.W., Liu, Q., Katrukha, E.A., Altelaar, A.F.M., Heck, A.J.R., Hoogenraad, C.C., and Akhmanova, A. (2014). Microtubule minus-end stabilization by polymerization-driven CAMSAP deposition. Dev. Cell *28*, 295–309. https://doi.org/10.1016/j.devcel.2014.01.001.
44. Goldstein, B., and Macara, I.G. (2007). The PAR proteins: fundamental players in animal cell polarization. Dev. Cell *13*, 609–622. https://doi.org/10.1016/j.devcel.2007.10.007.
45. Bloodgood, B.L., and Sabatini, B.L. (2005). Neuronal activity regulates diffusion across the neck of dendritic spines. Science *310*, 866–869.
46. Gulledge, A.T., Carnevale, N.T., and Stuart, G.J. (2012). Electrical advantages of dendritic spines. PLoS One *7*, e36007. https://doi.org/10.1371/journal.pone.0036007.
47. Svoboda, K., Tank, D.W., and Denk, W. (1996). Direct measurement of coupling between dendritic spines and shafts. Science (New York, N.Y.) *272*, 716–719. https://doi.org/10.1126/science.272.5262.716.
48. Yuste, R. (2013). Electrical compartmentalization in dendritic spines. Annu. Rev. Neurosci. *36*, 429–449. https://doi.org/10.1146/annurev-neuro-062111-150455.
49. Grutzendler, J., Kasthuri, N., and Gan, W.B. (2002). Long-term dendritic spine stability in the adult cortex. Nature *420*, 812–816. https://doi.org/10.1038/nature01276.
50. Trachtenberg, J.T., Chen, B.E., Knott, G.W., Feng, G., Sanes, J.R., Welker, E., and Svoboda, K. (2002). Long-term *in vivo* imaging of experience-dependent synaptic plasticity in adult cortex. Nature *420*, 788–794. https://doi.org/10.1038/nature01273.
51. Bourne, J., and Harris, K.M. (2007). Do thin spines learn to be mushroom spines that remember? Curr. Opin. Neurobiol. *17*, 381–386. https://doi.org/10.1016/j.conb.2007.04.009.
52. Hinton, V.J., Brown, W.T., Wisniewski, K., and Rudelli, R.D. (1991). Analysis of neocortex in three males with the fragile X syndrome. Am. J. Med. Genet. *41*, 289–294. https://doi.org/10.1002/ajmg.1320410306.
53. Wisniewski, K.E., Segan, S.M., Miezejeski, C.M., Sersen, E.A., and Rudelli, R.D. (1991). The Fra(X) syndrome: neurological, electrophysiological, and neuropathological abnormalities. Am. J. Med. Genet. *38*, 476–480. https://doi.org/10.1002/ajmg.1320380267.
54. Rudelli, R.D., Brown, W.T., Wisniewski, K., Jenkins, E.C., Laure-Kamionowska, M., Connell, F., and Wisniewski, H.M. (1985). Adult fragile X syndrome. Clinico-neuropathologic findings. Acta Neuropathol. *67*, 289–295. https://doi.org/10.1007/bf00687814.
55. He, C.X., and Portera-Cailliau, C. (2013). The trouble with spines in fragile X syndrome: density, maturity and plasticity. Neuroscience *251*, 120–128. https://doi.org/10.1016/j.neuroscience.2012.03.049.
56. Belichenko, P.V., Wright, E.E., Belichenko, N.P., Masliah, E., Li, H.H., Mobley, W.C., and Francke, U. (2009). Widespread changes in dendritic and axonal morphology in Mecp2-mutant mouse models of Rett syndrome: evidence for disruption of neuronal networks. J. Comp. Neurol. *514*, 240–258. https://doi.org/10.1002/cne.22009.
57. Armstrong, D.D. (1992). The neuropathology of the Rett syndrome. Brain Dev. *14*, S89–S98.
58. Nakai, N., Takumi, T., Nakai, J., and Sato, M. (2018). Common Defects of Spine Dynamics and Circuit Function in Neurodevelopmental Disorders: A Systematic Review of Findings From in Vivo Optical Imaging of Mouse Models. Front. Neurosci. *12*, 412. https://doi.org/10.3389/fnins.2018.00412.
59. Demarco, R.S., and Lundquist, E.A. (2010). RACK-1 acts with Rac GTPase signaling and UNC-115/abLIM in Caenorhabditis elegans axon pathfinding and cell migration. PLoS Genet. *6*, e1001215. https://doi.org/10.1371/journal.pgen.1001215.
60. Wang, S., Wang, T., Liu, T., Xie, R.G., Zhao, X.H., Wang, L., Yang, Q., Jia, L.T., and Han, J. (2020). Ermin is a p116(RIP) -interacting protein promoting oligodendroglial differentiation and myelin maintenance. Glia *68*, 2264–2276. https://doi.org/10.1002/glia.23838.
61. Nakayama, M., Goto, T.M., Sugimoto, M., Nishimura, T., Shinagawa, T., Ohno, S., Amano, M., and Kaibuchi, K. (2008). Rho-kinase phosphorylates PAR-3 and disrupts PAR complex formation. Dev. Cell *14*, 205–215.
62. Ye, Y.P., Jiao, H.L., Wang, S.Y., Xiao, Z.Y., Zhang, D., Qiu, J.F., Zhang, L.J., Zhao, Y.L., Li, T.T., Li, L., et al. (2018). Hypermethylation of DMTN promotes the metastasis of colorectal cancer cells by regulating the

actin cytoskeleton through Rac1 signaling activation. J. Exp. Clin. Cancer Res. *37*, 299. https://doi.org/10.1186/s13046-018-0958-1.

63. Andra, K., Nikolic, B., Stocher, M., Drenckhahn, D., and Wiche, G. (1998). Not just scaffolding: plectin regulates actin dynamics in cultured cells. Genes Dev. *12*, 3442–3451. https://doi.org/10.1101/gad.12.21.3442.
64. Zhang, H., Webb, D.J., Asmussen, H., Niu, S., and Horwitz, A.F. (2005). A GIT1/PIX/Rac/PAK Signaling Module Regulates Spine Morphogenesis and Synapse Formation through MLC. J. Neurosci. *25*, 3379–3388. https://doi.org/10.1523/jneurosci.3553-04.2005.
65. Haditsch, U., Leone, D.P., Farinelli, M., Chrostek-Grashoff, A., Brakebusch, C., Mansuy, I.M., McConnell, S.K., and Palmer, T.D. (2009). A central role for the small GTPase Rac1 in hippocampal plasticity and spatial learning and memory. Mol. Cell. Neurosci. *41*, 409–419. https://doi.org/10.1016/j.mcn.2009.04.005.
66. Lelieveld, S.H., Reijnders, M.R.F., Pfundt, R., Yntema, H.G., Kamsteeg, E.J., de Vries, P., de Vries, B.B.A., Willemsen, M.H., Kleefstra, T., Löhner, K., et al. (2016). Meta-analysis of 2,104 trios provides support for 10 new genes for intellectual disability. Nat. Neurosci. *19*, 1194–1196. https://doi.org/10.1038/nn.4352.
67. Meng, J., Meng, Y., Hanna, A., Janus, C., and Jia, Z. (2005). Abnormal long-lasting synaptic plasticity and cognition in mice lacking the mental retardation gene Pak3. J. Neurosci. *25*, 6641–6650. https://doi.org/10.1523/jneurosci.0028-05.2005.
68. Bienvenu, T., des Portes, V., McDonell, N., Carrié, A., Zemni, R., Couvert, P., Ropers, H.H., Moraine, C., van Bokhoven, H., Fryns, J.P., et al. (2000). Missense mutation in PAK3, R67C, causes X-linked nonspecific mental retardation. Am. J. Med. Genet. *93*, 294–298. https://doi.org/10.1002/1096-8628(20000814)93:4<294::aid-ajmg8>3.0.co;2-f.
69. Allen, K.M., Gleeson, J.G., Bagrodia, S., Partington, M.W., MacMillan, J.C., Cerione, R.A., Mulley, J.C., and Walsh, C.A. (1998). PAK3 mutation in nonsyndromic X-linked mental retardation. Nat. Genet. *20*, 25–30. https://doi.org/10.1038/1675.
70. Hayashi, M.L., Rao, B.S.S., Seo, J.S., Choi, H.S., Dolan, B.M., Choi, S.Y., Chattarji, S., and Tonegawa, S. (2007). Inhibition of p21-activated kinase rescues symptoms of fragile X syndrome in mice. Proc. Natl. Acad. Sci. USA *104*, 11489–11494. https://doi.org/10.1073/pnas.0705003104.
71. Nagy, D., Farkas, K., Armengol, L., Segura, M., Esi Zodanu, G.K., Csányi, B., Zimmermann, A., Vámos, B., and Széll, M. (2020). Further delineation of the phenotype of PAK3-associated x-linked intellectual disability: Identification of a novel missense mutation and review of literature. Eur. J. Med. Genet. *63*, 103800. https://doi.org/10.1016/j.ejmg.2019.103800.
72. Iida, A., Takano, K., Takeshita, E., Abe-Hatano, C., Hirabayashi, S., Inaba, Y., Kosugi, S., Kamatani, Y., Momozawa, Y., Kubo, M., et al. (2019). A novel PAK3 pathogenic variant identified in two siblings from a Japanese family with X-linked intellectual disability: case report and review of the literature. Cold Spring Harb. Mol. Case Stud. *5*, a003988. https://doi.org/10.1101/mcs.a003988.
73. Horn, S., Au, M., Basel-Salmon, L., Bayrak-Toydemir, P., Chapin, A., Cohen, L., Elting, M.W., Graham, J.M., Gonzaga-Jauregui, C., Konen, O., et al. (2019). De novo variants in PAK1 lead to intellectual disability with macrocephaly and seizures. Brain *142*, 3351–3359. https://doi.org/10.1093/brain/awz264.
74. Kernohan, K.D., McBride, A., Hartley, T., Rojas, S.K., Care4Rare Canada Consortium, Dyment, D.A., Boycott, K.M., and Dyack, S. (2019). p21 protein-activated kinase 1 is associated with severe regressive autism, and epilepsy. Clin. Genet. *96*, 449–455. https://doi.org/10.1111/cge.13618.
75. Harms, F.L., Kloth, K., Bley, A., Denecke, J., Santer, R., Lessel, D., Hempel, M., and Kutsche, K. (2018). Activating Mutations in PAK1, Encoding p21-Activated Kinase 1, Cause a Neurodevelopmental Disorder. Am. J. Hum. Genet. *103*, 579–591. https://doi.org/10.1016/j.ajhg.2018.09.005.
76. Fossati, M., Pizzarelli, R., Schmidt, E.R., Kupferman, J.V., Stroebel, D., Polleux, F., and Charrier, C. (2016). SRGAP2 and Its Human-Specific Paralog Co-Regulate the Development of Excitatory and Inhibitory Synapses. Neuron *91*, 356–369. https://doi.org/10.1016/j.neuron.2016.06.013.
77. Schmidt, E.R.E., Kupferman, J.V., Stackmann, M., and Polleux, F. (2019). The human-specific paralogs SRGAP2B and SRGAP2C differentially modulate SRGAP2A-dependent synaptic development. Sci. Rep. *9*, 18692. https://doi.org/10.1038/s41598-019-54887-4.
78. Shuai, Y., Lu, B., Hu, Y., Wang, L., Sun, K., and Zhong, Y. (2010). Forgetting is regulated through Rac activity in Drosophila. Cell *140*, 579–589. https://doi.org/10.1016/j.cell.2009.12.044.
79. Jiang, L., Mao, R., Zhou, Q., Yang, Y., Cao, J., Ding, Y., Yang, Y., Zhang, X., Li, L., and Xu, L. (2016). Inhibition of Rac1 Activity in the Hippocampus Impairs the Forgetting of Contextual Fear Memory. Mol. Neurobiol. *53*, 1247–1253. https://doi.org/10.1007/s12035-015-9093-6.
80. Liu, Y., Du, S., Lv, L., Lei, B., Shi, W., Tang, Y., Wang, L., and Zhong, Y. (2016). Hippocampal Activation of Rac1 Regulates the Forgetting of Object Recognition Memory. Curr. Biol. *26*, 2351–2357. https://doi.org/10.1016/j.cub.2016.06.056.
81. Zhang, H., Webb, D.J., Asmussen, H., and Horwitz, A.F. (2003). Synapse formation is regulated by the signaling adaptor GIT1. J. Cell Biol. *161*, 131–142. https://doi.org/10.1083/jcb.200211002.
82. Cervantes-Sandoval, I., Chakraborty, M., MacMullen, C., and Davis, R.L. (2016). Scribble Scaffolds a Signalosome for Active Forgetting. Neuron *90*, 1230–1242. https://doi.org/10.1016/j.neuron.2016.05.010.
83. Humbert, P.O., Dow, L.E., and Russell, S.M. (2006). The Scribble and Par complexes in polarity and migration: friends or foes? Trends Cell Biol. *16*, 622–630. https://doi.org/10.1016/j.tcb.2006.10.005.
84. Kojima, H., Rosendale, M., Sugiyama, Y., Hayashi, M., Horiguchi, Y., Yoshihara, T., Ikegaya, Y., Saneyoshi, T., and Hayashi, Y. (2019). The role of CaMKII-Tiam1 complex on learning and memory. Neurobiol. Learn. Mem. *166*, 107070. https://doi.org/10.1016/j.nlm.2019.107070.
85. Saneyoshi, T., Matsuno, H., Suzuki, A., Murakoshi, H., Hedrick, N.G., Agnello, E., O'Connell, R., Stratton, M.M., Yasuda, R., and Hayashi, Y. (2019). Reciprocal Activation within a Kinase-Effector Complex Underlying Persistence of Structural LTP. Neuron *102*, 1199–1210.e6. https://doi.org/10.1016/j.neuron.2019.04.012.
86. Cheng, J., Scala, F., Blanco, F.A., Niu, S., Firozi, K., Keehan, L., Mulherkar, S., Froudarakis, E., Li, L., Duman, J.G., et al. (2021). The Rac-GEF Tiam1 Promotes Dendrite and Synapse Stabilization of Dentate Granule Cells and Restricts Hippocampal-Dependent Memory Functions. J. Neurosci. *41*, 1191–1206. https://doi.org/10.1523/JNEUROSCI.3271-17.2020.
87. Gu, J., Firestein, B.L., and Zheng, J.Q. (2008). Microtubules in dendritic spine development. J. Neurosci. *28*, 12120–12124. https://doi.org/10.1523/JNEUROSCI.2509-08.2008.
88. Hu, X., Ballo, L., Pietila, L., Viesselmann, C., Ballweg, J., Lumbard, D., Stevenson, M., Merriam, E., and Dent, E.W. (2011). BDNF-induced increase of PSD-95 in dendritic spines requires dynamic microtubule invasions. J. Neurosci. *31*, 15597–15603. https://doi.org/10.1523/JNEUROSCI.2445-11.2011.
89. Hu, X., Viesselmann, C., Nam, S., Merriam, E., and Dent, E.W. (2008). Activity-dependent dynamic microtubule invasion of dendritic spines. J. Neurosci. *28*, 13094–13105. https://doi.org/10.1523/JNEUROSCI.3074-08.2008.
90. Meng, W., Mushika, Y., Ichii, T., and Takeichi, M. (2008). Anchorage of microtubule minus ends to adherens junctions regulates epithelial cell-cell contacts. Cell *135*, 948–959. https://doi.org/10.1016/j.cell.2008.09.040.
91. Nashchekin, D., Fernandes, A.R., and St Johnston, D. (2016). Patronin/Shot Cortical Foci Assemble the Noncentrosomal Microtubule Array that Specifies the Drosophila Anterior-Posterior Axis. Dev. Cell *38*, 61–72. https://doi.org/10.1016/j.devcel.2016.06.010.
92. Uchida, S., Martel, G., Pavlowsky, A., Takizawa, S., Hevi, C., Watanabe, Y., Kandel, E.R., Alarcon, J.M., and Shumyatsky, G.P. (2014). Learning-induced and stathmin-dependent changes in microtubule stability are critical for memory and disrupted in ageing. Nat. Commun. *5*, 4389. https://doi.org/10.1038/ncomms5389.
93. Fanara, P., Husted, K.H., Selle, K., Wong, P.Y.A., Banerjee, J., Brandt, R., and Hellerstein, M.K. (2010). Changes in microtubule turnover accompany synaptic plasticity and memory formation in response to contextual fear conditioning in mice. Neuroscience *168*, 167–178. https://doi.org/10.1016/j.neuroscience.2010.03.031.
94. Watson, J.L., Kruger, L.K., Ben-Sasson, A.J., Bittleston, A., Shahbazi, M.N., Planelles-Herrero, V.J., Chambers, J.E., Manton, J.D., Baker, D., and Derivery, E. (2023). Synthetic Par polarity induces cytoskeleton asymmetry in unpolarized mammalian cells. Cell *186*, 4710–4727.e35. https://doi.org/10.1016/j.cell.2023.08.034.
95. Reijnders, M.R.F., Ansor, N.M., Kousi, M., Yue, W.W., Tan, P.L., Clarkson, K., Clayton-Smith, J., Corning, K., Jones, J.R., Lam, W.W.K., et al. (2017). RAC1 Missense Mutations in Developmental Disorders with Diverse Phenotypes. Am. J. Hum. Genet.

101, 466–477. https://doi.org/10.1016/j.ajhg.2017.08.007.

96. Banka, S., Bennington, A., Baker, M.J., Rijckmans, E., Clemente, G.D., Ansor, N.M., Sito, H., Prasad, P., Anyane-Yeboa, K., Badalato, L., et al. (2022). Activating RAC1 variants in the switch II region cause a developmental syndrome and alter neuronal morphology. Brain *145*, 4232–4245. https://doi.org/10.1093/brain/awac049.
97. Voglewede, M., and Zhang, H. (2024). Loss of the polarity protein Par3 promotes dendritic spine neoteny and enhances learning and memory (Mendeley Data, V1). https://doi.org/10.17632/hdt3whx2bh.1.
98. Capaldo, C.T., and Macara, I.G. (2007). Depletion of E-cadherin disrupts establishment but not maintenance of cell junctions in Madin-Darby canine kidney epithelial cells. Mol. Biol. Cell *18*, 189–200.
99. Schindelin, J., Arganda-Carreras, I., Frise, E., Kaynig, V., Longair, M., Pietzsch, T., Preibisch, S., Rueden, C., Saalfeld, S., Schmid, B., et al. (2012). Fiji: an open-source platform for biological-image analysis. Nat. Methods *9*, 676–682. https://doi.org/10.1038/nmeth.2019.
100. Wilson, M.D., Sethi, S., Lein, P.J., and Keil, K.P. (2017). Valid statistical approaches for analyzing sholl data: Mixed effects versus simple linear models. J. Neurosci. Methods *279*, 33–43. https://doi.org/10.1016/j.jneumeth.2017.01.003.
101. Fiala, J.C. (2005). Reconstruct: a free editor for serial section microscopy. J. Microsc. *218*, 52–61. https://doi.org/10.1111/j.1365-2818.2005.01466.x.
102. Risher, W.C., Ustunkaya, T., Singh Alvarado, J., and Eroglu, C. (2014). Rapid Golgi analysis method for efficient and unbiased classification of dendritic spines. PLoS One *9*, e107591. https://doi.org/10.1371/journal.pone.0107591.
103. Gouveia, K., and Hurst, J.L. (2017). Optimising reliability of mouse performance in behavioural testing: the major role of non-aversive handling. Sci. Rep. *7*, 44999. https://doi.org/10.1038/srep44999.
104. Sun, M., Bernard, L.P., Dibona, V.L., Wu, Q., and Zhang, H. (2013). Calcium phosphate transfection of primary hippocampal neurons. J. Vis. Exp. e50808. https://doi.org/10.3791/50808.
105. Hendershott, M.C., and Vale, R.D. (2014). Regulation of microtubule minus-end dynamics by CAMSAPs and Patronin. Proc. Natl. Acad. Sci. USA *111*, 5860–5865. https://doi.org/10.1073/pnas.1404133111.
106. Pang, Z.P., Deng, P., Ruan, Y.W., and Xu, Z.C. (2002). Depression of fast excitatory synaptic transmission in large aspiny neurons of the neostriatum after transient forebrain ischemia. J. Neurosci. *22*, 10948–10957. https://doi.org/10.1523/jneurosci.22-24-10948.2002.
107. Retzbach, E.P., Sheehan, S.A., Krishnan, H., Zheng, H., Zhao, C., and Goldberg, G.S. (2022). Independent effects of Src kinase and podoplanin on anchorage independent cell growth and migration. Mol. Carcinog. *61*, 677–689. https://doi.org/10.1002/mc.23410.

STAR★METHODS

KEY RESOURCES TABLE

REAGENT or RESOURCE	SOURCE	IDENTIFIER
Antibodies		
Anti-Shank3	NeuroMAB	Clone N367/62; Cat#: 75-344; RRID: AB_2315921
Anti-Homer1	Synaptic Systems	Cat#: 160 003; RRID: AB_887730
Anti-GluR1	UC Davis	Clone: N355/1; Cat#: 73-327; RRID: AB_2315839
Anti-GluR2	Millipore	Clone: 6C4; Cat#: MAB397; RRID: AB_11212990
Anti-PSD-95	Antibodies Inc.	Clone: K28/43; Cat#: 75-028; RRID: AB_2292909
Anti-NMDAR1	BD Pharmingen	Cat#: 5563008; RRID: AB_396353
Anti-Rac1	Cytoskeleton, Inc.	Cat#: ARC03; RRID: AB_10709099
Anti-Phospho PAK	Cell Signaling Tehcnology	Cat#: 2606; RRID: AB_2299279
Anti-PAK	Santa Cruz	Cat#: 166887; RRID: AB_10609226
Anti-CAMSAP2	ProteinTech	Cat#: 17880-1-AP; RRID: AB_2068826
Anti-alpha-tubulin	DHSB	Cat#: AA4.3S; RRID: AB_579793
Anti-acetylated tubulin	Sigma	Clone: 6-11B-1; Cat#: MABT868; RRID: AB_2819178
Peroxidase-conjugated AffiniPure Goat Anti-Rabbit IgG	Jackson ImmunoResearch Laboratories, Inc.	Cat#: 111-035-003; RRID: AB_2313567
Peroxidase-conjugated AffiniPure Goat Anti-Mouse IgG	Jackson ImmunoResearch Laboratories, Inc.	Cat#: 115-035-003; RRID: AB_10015289
Anti-Synapsin	Millipore	Cat#: AB1543; RRID: AB_2200400
Anti-SV2	DSHB	Cat#: SV2-S; RRID: AB_2315387
Anti-GAPDH	Millipore	Clone: 6C5; Cat#: MAB374; RRID: AB_2107445
Anti-GFAP	Sigma	Clone: GA5; Cat#: MAB360; RRID: AB_11212597
Anti-IBA1	Wako	Cat#: 019-19741; RRID: AB_839504
Anti-LAMP2	Stress Marq	Clone: GL2A7; Cat#: SMC-141; RRID: AB_2281134
Anti-Par3	Millipore	Cat#: 07-330; RRID: AB_2101325
Anti-Phospho-aPKC	Cell Signaling Technology	Cat#: 9378; RRID: AB_2168217
Anti-PKCζ	Cell Signaling Technology	Clone: C24E6; Cat#: 9368; RRID: AB_10693777
Anti-PKCι/λ	Cell Signaling Technology	Clone: C83H11; Cat#: 2998; RRID: AB_2171737
Alexa Fluor 594 Donkey Anti-Rabbit	Invitrogen	Cat#: A21207; RRID: AB_141637
Bacterial and virus strains		
AAV-GFP	Addgene	Cat#: 105539-AAV9
AAV-Cre-GFP-hSyn	Addgene	Cat#: 105540-AAV9
Chemicals, peptides, and recombinant proteins		
Paraformaldehyde	Sigma	Cat#: P6148
Donkey serum	Sigma	Cat#: D9663
Poly-L-lysine	Sigma	Cat#: P2636
Critical commercial assays		
FD Rapid GolgiStain Kit	FD NeuroTechnologies	Cat#: PK401
Rac1 Pull-Down Activation Assay Biochem Kit	Cytoskeleton, Inc.	Cat#: BK035
Pierce 600nm Protein Assay Reagent	Thermo Scientific	Cat#: 22660
CalPhos™ Mammalian Transfection Kit	Takara	Cat#: 631312

(*Continued on next page*)

Continued

REAGENT or RESOURCE	SOURCE	IDENTIFIER
Deposited data		
Source data including phosphoproteomics	Mendeley Data	Mendeley Data: http://www.doi.org/10.17632/hdt3whx2bh.1[97]
Experimental models: Cell lines		
Rat2 fibroblasts	ATCC	Cat#: CRL-1764; RRID:CVCL_0513
Experimental models: Organisms/strains		
Mouse: *Pard3*$^{f/f}$: C57BL/6N-A^{tm1Brd}*Pard3*$^{tm1a(KOMP)Wtsi}$/HMmucd	MRC-Harwell	Cat#: 048974-UCD; RRID: MMRRC_048974-UCD
Mouse: flipase line: C57BL/6N-Tg(CAG-Flpo)1Afst/Mmucd	Mutant Mouse Resource & Research Centers	Cat#: 036512-UCD; RRID: MMRRC_036512-UCD
Mouse: *CaMKIIα-Cre*: Tg(Camk2a-cre)T29-1Stl	The Jackson Laboratory	Cat#: 005359; RRID: IMSR_JAX:005359
Mouse: Cre reporter: B6.129X1-*Gt(ROSA)26Sor*$^{tm1(EYFP)Cos}$/J	The Jackson Laboratory	Cat#: 006148; RRID: IMSR_JAX:006148
Mouse: Nestin-Cre: B6.Cg-Tg(Nes-cre)1Kln/J	The Jackson Laboratory	Cat#: 003771; RRID: IMSR_JAX:003771
Oligonucleotides		
Pard3 5arm-WTF (5′-CTGTTATCCTCCAAACCCTGA-3′)	Sigma Life Science	N/A
Pard3 Crit-WTR (5′-ACACTGGGAGAGACCACCAC-3′)	Sigma Life Science	N/A
Pard3 5arm-MutR (5′-GAACTTCGGAATAGGAACTTCG-3′)	Sigma Life Science	N/A
CaMKIIα-Cre Forward (5′-GAACCTGATGGAC ATGTTCAGG-3′)	Sigma Life Science	N/A
CaMKIIα-Cre Reverse (5′-AGTGCGTTCGAAC GCTAGAGCCTGT-3′)	Sigma Life Science	N/A
Recombinant DNA		
pFasBac+GFP-CAMSAP2	Addgene	Cat#: 59037; RRID: Addgene_59037
pEGFP-c1-CAMSAP2 WT	This paper	N/A
pEGFP-c1-CAMSAP2 S1019A	This paper	N/A
pEGFP-c1-CAMSAP2 S1019D	This paper	N/A
pK-mRFP	Ian Macara Lab	Capaldo and Macara[98]
Software and Algorithms		
FIJI	Schindelin et al.[99]	https://fiji.sc/; RRID: SCR_002285
GraphPad Prism v9	Graphpad Software Inc.	https://www.graphpad.com/; RRID: SCR_002798
Statistical Analysis System (SAS) 9.4	Statistical Analysis System	http://www.sas.com; RRID: SCR_008567
Mixed model SAS code	Wilson et al.[100]	https://doi.org/10.1016/j.jneumeth.2017.01.003
RECONSTRUCT	Fiala[101] Risher et al.[102]	http://synapses.clm.utexas.edu/tools/reconstruct/reconstruct.stm; RRID: SCR_002716
Clampfit	Molecular Devices	http://www.moleculardevices.com/products/software/pclamp.html; RRID: SCR_011323
Other		
Vectashield with DAPI	Vector Laboratories	Cat#: H-1200-10
Permount	Fisher Scientific	Cat#: SP15-100
Protease inhibitor cocktail	Sigma	Cat#: P8340
Phosphatase inhibitor cocktail	Sigma	Cat#: P0044
Minimum Essential Media Eagle	Sigma	Cat#: M2279
GlutaMAX	Gibco	Cat#: A12860-01
Sodium pyruvate	Gibco	Cat#: 11360-070
Penicillin/Streptomycin	Gibco	Cat#: 15070-063
DynabeadsProtein G	Thermo Fisher	Cat#: 10004D

(*Continued on next page*)

Continued

REAGENT or RESOURCE	SOURCE	IDENTIFIER
No-Stain Protein Labeling Reagent	Invitrogen	Cat#: A44449
Picrotoxin	Tocris	Cat#: 1128
D-AP5	Tocris	Cat#: 0106
Tetrodotoxin	HelloBio	Cat#: HB1035

RESOURCE AVAILABILITY

Lead contact

Further information and requests for resources and reagents should be directed to and will be fulfilled by the lead contact, Huaye Zhang (zhang29@rwjms.rutgers.edu).

Materials availability

Plasmids generated in this study are available upon request.

Data and code availability

- Data availability: All original source data including phosphoproteomics data can be found deposited at Mendeley Data and are publicly accessible as of the date of publication. The DOI for the original source data is listed in the key resources table.
- Code availability: This paper does not report original code.
- Any additional information required to reanalyze the data reported in this paper is available from the lead contact upon request.

EXPERIMENTAL MODEL AND STUDY PARTICIPANT DETAILS

Generation and genotyping of Pard3 conditional knockout line

To create the conditional knockout mouse line, we obtained C57BL/6N-A^{tm1Brd}*Pard3*$^{tm1a(KOMP)Wtsi}$/HMmucd (#048974-UCD) from MRC-Harwell. In this promoter driven construct line (Tm1a), a promotor driven cassette and a loxP site were inserted flanking exons 8 and 9 of *Pard3*. Exons 8 and 9 are expressed in all known variants of *Pard3*. Tm1a was crossed with a flippase line, C57BL/6N-Tg(CAG-Flpo)1Afst/Mmucd (MMRRC, 036512-UCD), removing the promoter driven cassette except for a loxP site, creating line Tm1c. When line Tm1c is crossed with a Cre line, Cre recombinase excises *Pard3* exons 8 and 9, rendering a nonfunctional Par3 protein. We crossed Tm1c with the CaMKIIα-Cre (Tg(Camk2a-cre)T29-1Stl; Jax#005359) to knockout Par3 in postnatal forebrain excitatory neurons during synaptogenesis. Tm1c line was also crossed with a Nestin-Cre line (B6.Cg-Tg(Nes-cre)1Kln/J; Jax#003771) for validation purposes. Genotypes were determined via PCR of DNA collected from ear or tail tissue. For the presence of floxed *Pard3*, the following primers were used: 5arm-WTF (5′-CTGTTATCCTC CAAACCCTGA-3′), Crit-WTR (5′-ACACTGGGAGAGACCACCAC-3′), and 5arm-MutR (5′-GAACTTCGGAATAGGAACTTCG-3′). For the presence of *CaMKIIα-Cre*, the following primers were used: Forward (5′-GAACCTGATGGACATGTTCAGG-3′) and Reverse (5′-AGTGCGTTC GAACGCTAGAGCCTGT-3′). Cre expression was validated by crossing the *Pard3* line with B6.129X1-*Gt(ROSA)26Sor*$^{tm1(EYFP)Cos}$/J. Mice were housed in a 12 hour dark/light cycle with *ad libitum* access to chow and water. Experiments were completed in male and female 5- to 7-week-old mice, unless otherwise indicated. All experiments are in compliance with the Rutgers University institutional animal care and use committee (IACUC) protocols.

METHOD DETAILS

Immunohistochemistry

Mice were deeply anesthetized with 1.2% avertin and then perfused with 1x Phosphate Buffered Saline (PBS) and 4% paraformaldehyde (PFA) (Sigma, P6148). Brains were removed and postfixed in 4% PFA at 4°C for 12 to 18 hours. Brains were transferred to a 20 to 30% sucrose gradient at 4°C. Brains were flash froze in pre-chilled -80°C isopentane and sectioned at 30μm using a cryostat (Leica, CM1900). For immunohistochemistry, all steps were completed at room temperature. Sections were blocked rocking for 1 hour in blocking solution (10% donkey serum (Sigma, D9663) in 1x PBS with 0.3% Triton-X 100). Primary antibody (Anti-Par3, 1:500, Millipore 07-330) was added directly to the blocking solution and incubated for 12 to 18 hours while rocking. Sections were washed 3 x 5 minutes in 1x PBS. Sections were incubated for 1 hour in secondary antibody (Alexa Fluor 594 Donkey Anti-Rabbit, 1:250, Invitrogen, A21207) in 1x PBS with 0.3% Triton-X 100 and 4% donkey serum (Sigma, D9663). Sections were washed 3 x 5 minutes in 1x PBS before being mounted on positive charged slides in Vectashield with DAPI (Vector Laboratories, H-1200-10) and imaged using an Olympus FV1000MPE microscope using a UMPLFLN 10X objective (N.A. 0.3).

Golgi staining, imaging, and analysis

Brains were processed using FD Rapid GolgiStain kit (FD NeuroTechnologies, Inc., PK401) per manufacturer's directions. Briefly, mice were deeply anesthetized with 1.2% Avertin. After non-response to tail and toe pinch, mice were decapitated. The brain was removed and placed in

Solution A + B mixed 24 hours prior. After an overnight incubation at room temperature in the dark, the Solution A + B was changed. After a 3-week total incubation in the dark, the brain was transferred to Solution C for 72 hours with a change after 24 hours. Brains were rapidly frozen in pre-chilled isopentane for 5 minutes on dry ice and stored at -80°C until sectioning. 200μm sections were cut using a Cryostat (Microm HM505E) and plated on gelatin coated slides. After drying overnight in the dark the tissue was rinsed twice in ddH_2O, stained with diluted Solution D + E, rinsed twice in ddH_2O, dehydrated in 50%, 75%, 95% ethanol, further dehydrated four times in 100% ethanol, cleared thrice in xylene, and coverslipped with Permount (Fisher Scientific, SP15-100). Z-stack images were collected at 0.25 μm thickness using either a Leica DMRE using the Hamamatsu ORCA-ER camera and Leica 506185 63x objective or Axio Imager M1 Zeiss using the ZxioCam MRM camera, AxioVision Rel. 4.8 program, and 100X Plan-APOCHROMAT 100X/1,40:|DIC infinity/0.17 objective. Images were processed and dendritic spines analyzed in FIJI[99] and RECONSTRUCT.[101,102] Morphology categorical cutoffs were used as previously described.[102] Briefly, spines were included in the first category they fit into in the following hierarchical order. First, "branched" spines were manually labeled. Second, filopodia spines had a length greater than 2 μm. Third, mushroom spines had a length to width ratio (LWR) greater than 0.6. Fourth, long thin spines had a length greater than 1 μm. Fifth, thin spines had a LWR greater than 1. Lastly, stubby spines had a LWR less than 1. Outliers were calculated and removed according to ROUT with Q value of 1%.

Behavior

All mice were handled for 3 days prior to the start of behavioral tests. A handling tunnel was used to minimize stress.[103] Mice were moved to the testing room at least 30 minutes prior to experimentation on all behavioral test days. All apparatuses were cleaned with 70% ethanol after each mouse.

Morris Water Maze (MWM)

The MWM pool is 1.3 meter in diameter filled with opaque water maintained at 21 ± 1°C. During testing the cages were placed on a warming pad. During the 4 training days mice received 3 or 5 trials per day with at least 15-minute intertrial intervals. The trial starting location pattern was never repeated across the 4 training days. Mice were released into the water facing the pool wall and were guided to the platform if they do not reach it within 60 seconds. Mice remained on the platform for 15 seconds before being retrieved. On day 5, the probe test is completed by removing the platform, releasing the mice from a novel location, and allowing the mice to swim for 60 seconds. Latency to platform, time in quadrant, velocity, number of platform crossings, and cumulative distance from platform were measured using EthoVision XT.

Elevated Plus Maze (EPM)

The EPM apparatus was 56 cm above the ground. The arms were 5 cm wide and 25 cm long. The enclosed arms had 16 cm high walls. Mice were placed in the center of the apparatus and allowed to freely explore for 10 minutes. Time spent in the open arm, number of entries into the open arm, distance traveled, and velocity were measured using ANY-maze.

Open Field Test (OFT)

The OFT was conducted in a 40 cm x 40 cm x 40 cm white plexiglass box with a light positioned directly above the apparatus. Mice were placed in the center of the apparatus and allowed to freely explore for 10 minutes. Time spent in the outer edge of the field, number of entries into the outer edge, distance traveled, and velocity were measured using ANY-maze. Grooming, rearing, and jumping were manually scored by a blinded observer in ANY-maze.

Marble burying

Mice were separated into single cages 3 days before testing. 5 cm of pelleted cellulose bedding was placed in a large cage (36cm x 27cm) with a grid of 4 x 5 marbles placed on top. Mice were placed in the cage and allowed to explore for 30 minutes. Marbles >2/3 buried were manually counted. Marbles were cleaned with 70% ethanol and fresh pelleted cellulose bedding was replaced before each test.

Sociability

In the 3 chambers apparatus (59cm width x 29cm depth x 40cm height) two wire mesh cups (10cm in diameter x 16cm) were placed in opposite corners of the apparatus. The wire mesh cups were covered with 15cm plastic petri dishes to discourage the mice from climbing on top of the cup. On the first day mice were habituated to the apparatus and empty cups by exploring for 10 minutes. 24 hours later mice underwent the sociability test. A sex- and age-matched stranger mouse was placed in one of the wire mesh cups. The experimental mouse was placed in the center chamber and allowed to explore the 3 chambers for 10 minutes. Amount of time in each chamber and interaction time with each wire cup were calculated using ANY-maze. The compartment preference index was calculated by subtracting the time in the empty compartment from the time in stranger compartment divided by the total time spent in both the stranger and empty compartment. The interacting preference index was calculated by subtracting the time spent interacting with the empty cup from the stranger cup divided by the total time spent interacting with both cups.

Primary neuronal culture and fluorescent recovery after photobleaching (FRAP) imaging

Cultures were harvested and maintained as previously described.[104] For *Pard3* line validation, $Pard3^{f/f}$ males and females were bred. Cortical neurons were harvested from E17.5 embryonic brains. High density cultures were seeded at $8.5x10^5$ cells per 35 mm dish coated

with 0.1 mg/mL poly-L-lysine (Sigma, P2636). At DIV0 cells were infected with either AAV-Cre-GFP-hSyn (Addgene, 105540-AAV9) or AAV-GFP (Addgene, 105539-AAV9). At DIV14, neurons were lysed in RIPA buffer containing 20mM Tris-HCl pH 7.4, 150mM NaCl, 0.5% NP-40, 1.0% Triton-X-100, 2 mM EDTA, 2mM EGTA, 0.25% NaDOC, supplemented with protease inhibitor cocktail (Sigma, P8340) and phosphatase inhibitor cocktail (Sigma, P0044). Lysates were cleared at 16,100 x g for 10 minutes at 4°C and analyzed via Western Blot. For GFP-CAMSAP2 live imaging, hippocampal neurons were harvested from E18 rat embryonic brains. Neurons were seeded at 18,000 cells per 15 mm circular glass coverslip coated with 1mg/mL poly-L-lysine. At DIV3-4 neurons were co-transfected with mRFP, a gift from Ian Macara,[98] and GFP-CAMSAP2 WT, S1019A, or S1019D using the CalPhos™ Mammalian Transfection Kit (Takara, 631312) as previously described.[104] pFasBac+GFP-CAMSAP2 was a gift from Ron Vale (Addgene, # 59037, RRID:Addgene_59037)[105] and subcloned into the pEGFP-c1 backbone. pEGFP-c1-CAMSAP2 S1019A and S1019D were generated via site directed mutagenesis. Live images of dendrites were captured at DIV6-8 using an Olympus FV1000MPE microscope and Olympus LUMPlanFL N 60x objective N.A. 1.00. Fluorescent recovery after photobleaching (FRAP) was completed using the tornado photobleaching function in Olympus Fluoview version 4.2c. Fluorescent recovery was calculated as the corrected fluorescent intensity: (bleached region - background) / (unbleached region - background) across time. The fluorescent recovery was fitted using the exponential recovery function in the curve fitter tool in FIJI[99] to determine slow recovery and fraction immobile. Outliers were calculated and removed according to ROUT with Q value of 1%.

Cell culture and CAMSAP2 length quantification

Rat2 fibroblasts (ATCC, CRL-1764) were maintained in Minimum Essential Media Eagle (Sigma, M2279), supplemented with 5% fetal bovine serum, 5% calf serum, 0.6% glucose, 2mM GlutaMAX (Gibco, A12860-01), 1mM sodium pyruvate (Gibco, 11360-070), and 50U/ml Penicillin/Streptomycin (Gibco, 15070-063). Cells were co-transfected with mRFP and GFP-CAMSAP2 WT, S1019A, or S1019D using Lipofectamine 2000 (Invitrogen, 11668-019) in serum free media. Cells were imaged 18-24 hours post transfection with an Olympus FV1000MPE microscope (Olympus LUMPlanFL N 60x objective N.A. 1.00). GFP-CAMSAP2 length was measured using FIJI.[99]

Synaptosomal fractionation

For all synaptosomal fractions, co-immunoprecipitations, and Rac activity assays, mice were euthanized via cervical dislocation and the hippocampi were dissected in ice-cold 1xPBS and flash frozen on dry ice. For synaptosomal fractionation, tissue was homogenized in 10mM HEPES pH 7.4, 2mM EDTA, protease inhibitor (Sigma, P-8340), and phosphatase inhibitor (Sigma, P0044) using a 2 mL glass douncer and incubated on ice for 10 minutes. Lysates were centrifuged for 10 minutes at 1,000 x g and 4°C creating the P1 nuclei pellet and S1 homogenate supernatant. The S1 homogenate supernatant was separated and centrifuged for 15 minutes at 10,000 x g and 4°C creating the S2 cytosolic supernatant and the P2 crude synaptosome pellet. S2 was removed. P2 was resuspended in 50mM HEPES pH 7.4, 2mM EDTA, 2mM EGTA, 1% Triton-X-100, protease inhibitor (Sigma, P-8340), and phosphatase inhibitor (Sigma, P0044). Resuspended P2 was centrifuged for 80 minutes at 20,000 x g and 4°C creating the S3 vesicular/presynaptic supernatant and the P3 PSD-enriched pellet (Figure S2C). P3 was resuspended in 100mM Tris pH 9, 1% sodium deoxycholate, 0.025% SDS, protease inhibitor cocktail (Sigma, P-8340), and phosphatase inhibitor cocktail (Sigma, P0044). Fraction concentrations were measured with Pierce 600nm Protein Assay Reagent (Thermo Scientific, 22660) and prepared in Laemmli's sample buffer.

Rac activity assay

Rac1 activity was determined using the Rac1 Pull-Down Activation Assay Biochem Kit (Cytoskeleton, Inc., BK035), following manufacturer's protocol. Briefly, 300 μg of hippocampal lysate was incubated with 10 μg of GST-tagged PAK-PBD beads, washed, and analyzed via Western Blot. For positive and negative controls 300 μg of lysate was incubated with either GTPγS or GDP, respectively, for 15 minutes at room temperature immediately prior to incubation with GST-PAK-PBD beads.

Co-immunoprecipitation

For co-immunoprecipitation (co-IP), hippocampi were lysed in co-IP lysis buffer (20mM Tris-HCl, 137mM NaCl, 2mM EDTA, 1% NP-40, supplemented with protease and phosphatase inhibitor cocktails). Lysates were incubated on ice for 10 minutes prior to collecting 5% for input sample. 1μg of Anti-CAMSAP2 (ProteinTech, 17880-1-AP) was added to 200μg of lysate and nutated at 4°C for 1 hour. Dynabeads Protein G (Thermo Fischer, 10004D) were added to the lysate and nutated at 4°C for 1 hour. The Dynabeads were washed 3 times (20mM Tris-HCl, 137mM NaCl, 2mM EDTA) at 4°C before eluting with SDS sample buffer.

Western blot

Protein levels were analyzed via Western Blot analysis. Synaptosomal protein expression levels were normalized to total protein using No-Stain Protein Labeling Reagent (Invitrogen, A44449). Primary antibodies (see Table S3) were diluted in 1 x PBS + 0.15% (v/v) Tween-20 and 3% (w/v) bovine serum albumin. Secondary antibodies (Peroxidase-conjugated AffiniPure Goat Anti-Rabbit IgG, 1:5,000, Jackson ImmunoResearch Laboratories, Inc., 111-035-003; Peroxidase-conjugated AffiniPure Goat Anti-Mouse IgG, 1:5,000, Jackson ImmunoResearch Laboratories, Inc., 115-035-003) were diluted in 1 x PBS + 0.15% Tween-20 and 3% (w/v) bovine serum albumin. Densitometry was measured using FIJI.[99]

Electrophysiology

Brain slice physiology was performed in the dorsal CA1 pyramidal neurons in 5-7-week-old mice as described previously with some modifications.[106] Mice were anesthetized and euthanized by intracardial perfusion with ice-cold cutting solution (125mM NaCl, 25mM $NaHCO_3$, 2.5mM KCl, 1.25mM NaH_2PO_4, 2mM $CaCl_2$, 10mM $MgCl_2$, 2.5mM glucose) oxygenated with 95% O_2/5% CO_2. 300 μm sagittal sections were cut in ice-cold cutting solution oxygenated with 95% O_2/5% CO_2. Slices were transferred to cutting solution at 33°C for 10 minutes and then to a second warm beaker filled with ACSF (125mM NaCl, 25mM $NaHCO_3$, 2.5mM KCl, 1.25mM NaH_2PO_4, 2.5mM $CaCl_2$, 1.2mM $MgCl_2$, and 2.5mM glucose) oxygenated with 95% O_2/5% CO_2. Post 1 hour recovery, sections were perfused continuously at 4 mL/minute with oxygenated ACSF plus 22.5mM sucrose in a recording chamber at room temperature (~30°C). During recordings, a CA1 neuron was held at -70mV and recorded in voltage-clamp mode for 3-5 minutes while in ACSF 50μM picrotoxin (Tocris, 1128), 40μM D-AP5 (Tocris, 0106), and 1μM tetrodotoxin (HelloBio, HB1035). Traces were analyzed in Clampfit (Molecular Devices) and filtered using a lowpass boxcar filter with 11 smoothing points with a manual template search for mEPSCs. Events below 10 pA were excluded. Amplitudes were determined by averaging all events in a single recording.

Phosphoproteomic analysis

Hippocampal tissue was lysed in 8M Guanidine HCl, 50mM Tris, pH7.5, 5mM DTT and processed for phosphoproteomic analysis as previously described.[107] Database for Annotation, Visualization, and Integrated Discovery (DAVID)[35,36] was used to analyze molecules based on Functional GO Analysis.

QUANTIFICATION AND STATISTICAL ANALYSIS

For manual measurements samples were blinded at both collection and analysis. Multiple data points collected within the same animal or cell were analyzed in Statistical Analysis System 9.4 (SAS) using a mixed model with simple covariance to nest multiple measurements within subjects as previously described.[100] All other data sets were analyzed in Prism GraphPad using an unpaired T-Test or two-way ANOVA with Šídák's or Tukey's multiple comparison tests. Graphs were made in GraphPad Prism. Bar graphs depict individual measurements as data points and mean ± standard error of the mean (SEM). Violin plots depict thick lines as median and dotted lines as quartiles. Sample size details are listed in figure legends. Statistical significance was set at $p \leq 0.05$.